frontiers | Frontiers in Marine Science

TYPE Original Research
PUBLISHED 28 April 2023
DOI 10.3389/fmars.2023.1156915

Check for updates

OPEN ACCESS

EDITED BY
Wei-Bo Chen,
National Science and Technology Center for Disaster Reduction (NCDR), Taiwan

REVIEWED BY
Huamao Yuan,
Institute of Oceanology, Chinese Academy of Sciences (CAS), China
Limin Hu,
Ocean University of China, China

*CORRESPONDENCE
James T. Liu
james@mail.nsysu.edu.tw

RECEIVED 02 February 2023
ACCEPTED 17 April 2023
PUBLISHED 28 April 2023

CITATION
Lee J, Liu JT, Lin Y-S, Chen C-TA and Wang B-S (2023) The contrast in suspended particle dynamics at surface and near bottom on the river-dominated northern South China Sea shelf in summer: implication on physics and biogeochemistry coupling.
Front. Mar. Sci. 10:1156915.
doi: 10.3389/fmars.2023.1156915

The contrast in suspended particle dynamics at surface and near bottom on the river-dominated northern South China Sea shelf in summer: implication on physics and biogeochemistry coupling

Jay Lee[1], James T. Liu[1*], Yu-Shih Lin[1], Chen-Tung Arthur Chen[1] and Bo-Shian Wang[2,3]

[1]Department of Oceanography, National Sun Yat-sen University, Kaohsiung, Taiwan, [2]National Academy of Marine Research, Ocean Affairs Council, Kaohsiung, Taiwan, [3]Taiwan Ocean Research Institute, National Applied Research Laboratories, Kaohsiung, Taiwan

To understand the process-response relations among physical forcing and biogeochemical properties of suspended particles (SPs) in the river-dominated northern South China Sea shelf, a 5-day shipboard observation was conducted at a fixed location on the dispersal pathway of the Zhujiang (Pearl) River plume (ZRP) in the summer of 2016. Instrumented moorings were deployed near the sampling site to record the flow and wave fields every 10 minutes. Hydrographic properties were measured hourly to identify different water masses. Water and SPs samples at the surface (3 m) and near the bottom (3 m above the bed) were taken every 3 h for the analyses of nutrients, chlorophyll-a (Chl-a), and particulate organic matter (POM including POC, PN, and $\delta^{13}C_{POC}$). Meanwhile, the grain-size composition of SPs and seafloor sediment were also analyzed. Results showed that monsoon winds drove cold upwelling and ZRP waters at the surface. Both the upwelling and ZRP regimes contained newly produced marine phytoplankton based on low POC/Chl-a ratio (PC ratio) and enriched $\delta^{13}C_{POC.}$ However, SPs in the ZRP regime were smaller (<153 μm), having denser particle bulk density, and less enriched $\delta^{13}C_{POC}$, indicating different bio-communities from the upwelling regime. EOF analysis of the surface data suggested that mixing processes and the dispersal of the ZRP regime were mainly controlled by far-field storm winds, tidal modulation, and strength of mixing. On the other hand, a bottom nepheloid layer (BNL) was observed, mainly consisting of SPs<63 μm with higher bulk density than SPs at the surface. POM in the BNL was degraded and $\delta^{13}C_{POC}$-depleted according to the PC ratio and $\delta^{13}C_{POC}$. EOF analysis of the near-bottom data indicated that the dominant physical processes influencing the biogeochemical properties of SPs in the BNL were jointly the upwelling-associated lateral transport (first order) and tide-related resuspension (second order). Our study identified the contrast between the surface and near-bottom regimes with the coupling patterns among physical forcing and physiochemical properties of SPs using good constraints on particle dynamics and particle sources.

KEYWORDS

Zhujiang River (Pearl River) plume, benthic nepheloid layer (BNL), far-field storm wind, tidal modulation, landward transport, PC ratio, particulate organic matter

1 Introduction

RiOMars systems (river-dominated ocean margins; McKee et al., 2004) receive a variety of terrestrial and marine substances delivered by rivers or coastal currents (Mittelstaedt, 1991; Lacan and Jeandel, 2005; Jeandel, 2016; Liu et al., 2021). The diversity of particles in these systems includes bio-aggregates or flocs on the Amazon shelf (Gibbs, 1977; Nittrouer and DeMaster, 1996; Berhane et al., 1997), terrestrially-derived organic carbon from the Mississippi River (Bianchi et al., 2007), and lithogenic particles delivered from the Changjiang (Yangtze) River (Jiang et al., 2015; Liu et al., 2021). Terrestrial particles are initially dispersed from the river mouth (Wright and Nittrouer, 1995) and carried by the river plume, which generally contains abundant nutrients that enhance the phytoplankton production in the coastal sea (Yin et al., 2001; Isobe and Matsuno, 2008; Xu et al., 2008; Yang et al., 2021). The delivered particles follow a source-to-sink pathway of initial deposition, then resuspension and lateral transport (physical processes), which lead to the final accumulation and burial (sink) (Wright and Nittrouer, 1995). Meanwhile, the offshore marine dissolved (e.g., nutrients) and particulate matters could be carried inshore by landward currents as part of the upwelling circulation (D'Croz and O'Dea, 2007; Lu et al., 2010; Gao et al., 2018; Yang et al., 2021). Therefore, the physiochemical properties of suspended particles (SPs) are complex because of complicated particle dynamics occupying the water column in the coastal region (Dagg et al., 2004; McKee et al., 2004; Liu et al., 2021).

The physicochemical characteristics of SPs undergo transformation while en route, which influences the nature of particles (Turner and Millward, 2002; McKee et al., 2004; Liu et al., 2021). Three direct or indirect processes are involved, including water-particle interactions (e.g., flocculation/deflocculation; Gibbs and Konwar, 1986; Lee et al., 2016; Du et al., 2021); benthic sediment processes (e.g., resuspension; Thorne et al., 2009; O'Hara Murray et al., 2012); and biological processes (e.g., egestion and excretion; Turner and Millward, 2002; Myklestad, 2005; Castillo et al., 2010). For example, water mixing facilitates aggregation of biogenic substances (e.g., transparent exopolymer particles) with inorganic terrestrial particles to obtain high bulk densities (Passow et al., 2001; Ho et al., 2022). Then, the aggregated substances settle to the seafloor because of the ballast effect (McKee et al., 2004; Passow et al., 2014; Rixen et al., 2019). Next, the aggregated particles on the seabed are re-disturbed by current-induced or wave-induced turbulence and become sorted according to the corresponding density and size (Jarvis et al., 2005; Liu et al., 2021; Tian Z. et al., 2022).

Therefore, the physicochemical properties of the SP are conventionally used as indicators or proxies because particles are imprinted with the properties of the ambient environment in the transport processes (Gibbs, 1973; Linders et al., 2018; Liu et al., 2021; Lee et al., 2022). Particulate organic matter (POM) is prevalent in determining the source of SPs and reconstructing the biogeochemical pathways in two-end member systems (Guo et al., 2019; Liu et al., 2021). The relation between the organic carbon stable isotope ratio ($\delta^{13}C_{POC}$) and C/N (atomic carbon and nitrogen ratio) was utilized to identify signatures of terrestrial plants and marine algae (Lamb et al., 2006). The high Chl-a concentration at the surface of the oligotrophic ocean was regarded as an indication of the upwelling water mass, which carries nutrients from the subsurface water (Xu et al., 2009; Liu et al., 2019).

However, the low weight proportion of the POM and the bio-decomposition could affect the reliability of the source identification, which increases the difficulty of deciphering the target's provenance (Asada et al., 2005; Harrison et al., 2008; Guo et al., 2015). Thus, multiple measurements of different attributes must be applied to constrain the source interpretation of SPs. For instance, the high Chl-a concentration in the coastal region links to the phytoplankton growth, which could result from the eutrophication related either to upwellings or river runoff (Dickson and Wheele, 1995; Yin et al., 2001; Hong et al., 2009; Liu et al., 2019). The origin can be distinguished according to the nutrient composition because upwellings usually carry a high silicate concentration, whereas river runoffs always have a high N/P ratio (the ratio of inorganic total N to phosphate; Malakoff, 1998; Yin et al., 2001). One of the physical characteristics of the particle, particle bulk density, is also applicable to identifying the species of the SP (e.g., fluffy flocs, biogenic particles, and solid detrital; Hsu and Liu, 2010; Lee et al., 2016; Du et al., 2022). With corresponding observations of flow fields, salinity, and temperature, the physical mechanisms and water masses that transport SPs can be determined (Liu et al., 2019).

The SP in the northern South China Sea (NSCS) shelf was targeted in this study because of the various origins of particles. The largest terrestrial source is the Zhujiang (Pearl) River, of which the annual river discharge is $3.3 \times 10^{11} m^3\ yr^{-1}$ with annual sediment load of 64.5 Mt (Wu et al., 2012). Almost 80% of the river runoff occurs in the wet season (Zhang et al., 2012; Wu et al., 2016). Land-sourced substances are carried northeastward by the Zhujiang river plume (ZRP) in the surface due to the wind-driven current parallel to the Guangdong coastline in summer (Zu and Gan, 2015). Different approaches have been used to identify the dispersing ZRP (Chen et al., 2017; Zhi et al., 2022). According to the *in-situ* hydrographic measurements, the ZRP was recognized as low salinity water with a high N/P ratio (Yin et al., 2001; Yu et al., 2020). Satellite images show that a band-shaped Chl-a pattern from the Zhujiang river mouth dispersed into the N-limited NSCS, further spreading into the southern Taiwan Strait (Yin et al., 2001; Bai et al., 2015). Another well-known physical process that transports particles in the NSCS is the upwelling circulation which can be recognized as the low sea-surface temperature along the Guangdong coast (Chen et al., 2017; Zhang et al., 2018). The upwelling system is a substantial nutrient pump in the coastal region for the marine food web and enhances the biomass and the particulate organic flux (Kämpf and Chapman, 2016; Zhang et al., 2019).

Although previous research has studied the spatial distribution of biogeochemical properties of SPs on the inner shelf of the NSCS (Yu et al., 2010; Guo et al., 2015; Cao et al., 2020; Huang et al., 2021), the interpretation of these observations may be subject to aliasing over time due to hydrodynamic forcing such as tidal flows. Furthermore, the influence of the physical forcing on the biogeochemical properties of SPs has yet to be well-established in the existing literature. Therefore, our work intends to characterize and quantify the temporal coupling between physical forcing and the biogeochemistry of SPs on the NSCS shelf in summer. This study focuses on contrasting regimes of physical processes, water masses, and SPs from diverse origins on the pathway of the ZRP dispersal. Interdisciplinary approaches were designed to constrain the source of the SP, based on the observation by Lee et al. (2021). We aim to elucidate the source-to-sink nature of the particle transport pathways and improve the knowledge of particle dynamics, including the sediment routing systems (Wright and Coleman, 1973; Gao et al., 2015; Liu et al., 2016; Zhong et al., 2017), sedimentology (Kuehl et al., 1986; Heise et al., 2013; Zhang et al., 2013), and biogeochemical cycles (Cai et al., 2004; Bauer et al., 2013; Wei et al., 2020) in the river-dominated environments on the continental shelf.

2 Material and methods

2.1 Hydrodynamic measurements

R/V Ocean Researcher I was used for the fieldwork on July 24-29, 2016, at Sta. ZHJ2, where the average water depth was ~41 m (Figure 1A). Two taut-line moorings were deployed nearby to record the wave and flow fields (Figure 1B). One mooring was mounted with an AQUAdopp (at 8 m) whose wave mode had 10 minute-bursts, each containing wave height, period, and incident angle averaged over 512 measurements sampled at 1 Hz. WAVEWATCH III (Tolman, 1991) was used for the quality control of the *in-situ* wave measurement (Supplementary Figure 1). The upward-looking AQUAdopp had a bin size of 0.1 m with a central frequency of 1 MHz. The other mooring was mounted with two RDI ADCPs, one upward-looking (1,200 kHz) at 11 m below the surface and the other downward-looking (300 kHz) at 30 m above bed. The sampling rate for both ADCPs was 10 min (Supplementary Table 1).

The measured flow field was separated into tidal and non-tidal contributions. Using a MATLAB program *t_tide* (Pawlowicz et al., 2002), the tidal part of the flow at the study site was reconstructed through harmonic analysis. The non-tidal part of the flow was extracted after removing the tidal part from the measured flow. The tidal and non-tidal flows were then decomposed into the alongshore and across-shore/on-offshore components by orienting measured flows 15 degrees counterclockwise in the Cartesian coordinate. The NE-ward and inshore directions were defined as positive in the alongshore and across-shore flows, respectively. Flow measurements were used to derive the progressive vectors (PVs), of which the equation is shown in Section 3. The shear velocity (u_*) was calculated using flow and wave field measurements through the Sedtrans05 model (Neumeier et al., 2008; Supplementary Table 1).

2.2 Shipboard profiling

Hourly hydrographic profiles were conducted using the SBE 911plus CTD rosette that included salinity, temperature, fluorescence, and light transmission (Supplementary Table 1). The sampling rate was 0.04 seconds (sec) at the CTD lowering rate of 0.5 m s^{-1}. A laser *in-situ* scattering and transmissometry, LISST-100X, was co-mounted on the rosette to measure volume concentrations (VCs) of SPs from 2.5 to 500 µm grain-size classes, which were classified into<63, 63-153, and >153 µm size groups for further analyses. Each VC record was the average of 10 measurements with a sampling rate of<0.23 sec. The corresponding depth to the VC was converted from the CTD record based on the measuring time of both instruments. The LISST-100X was calibrated by conducting the blank intensity of VCs recorded in the Milli-Q water (Millipore Academic A10) before the cruise.

2.3 Water sample collection and analyses

Water samples were taken every 3 hours (h) at 3 m below the surface and 3 m above the seabed (mab) using Niskin bottles mounted on the CTD rosette for the measurements of nutrients (N, P, and Si), suspended sediment concentration (SSC), Chl-a, and POM (POC, PN, and $\delta^{13}C_{POC}$; Supplementary Table 2). For nutrient analysis, 100 mL seawater was filtered through a 0.45 µm Millex®-LCR syringe filter and then added with the saturated $HgCl_2$ to kill the bacteria and algae. To identify the size composition of the bulk SSC, a nested filtration system, Catnet, was used onboard to filter 20 L seawater into 100 mL PE bottles through sieves having the mesh sizes of 10, 63, and 153 µm (Hsu and Liu, 2010; Lee et al., 2016; Du and Liu, 2017; Wen et al., 2018; Yang et al., 2021). Samples for Chl-a and POM analyses were separately collected in 500 mL

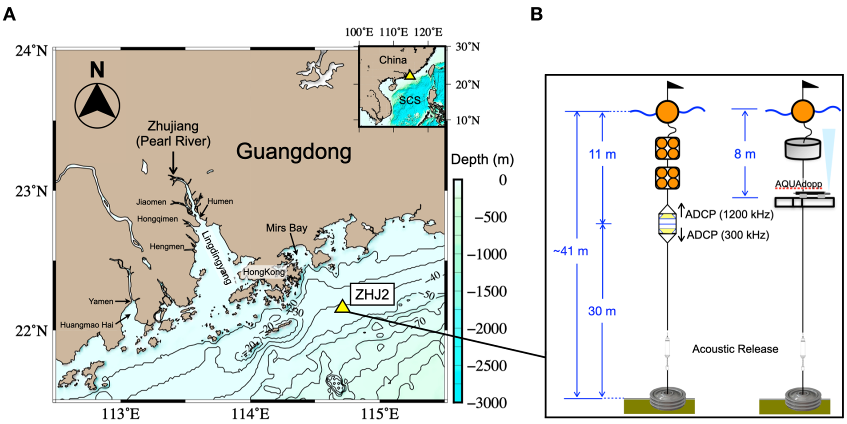

FIGURE 1
(A) A map showing the study site (ZHJ2; yellow triangles) in the northern South China Sea (insert). **(B)** A schematic diagram for the configuration of moorings deployed nearby ZHJ2 in July 2016. The map was plotted using the Generic Mapping Tools (GMT, V5.4.2, https://www.soest.hawaii.edu/gmt/).

opaque amber bottles. Those collected water samples were immediately filtered on the pre-combusted glass fiber filters (GF/F, Whatman; diameter: 25 mm; pore size: 0.7 μm; pre-combusted at 500°C for 6 h). Filters for Chl-a analysis were amended with a few drops of saturated $MgCO_3$ and wrapped in aluminum foil to prevent photodegradation. All samples were preserved at -20°C until analysis.

Upon returning to the laboratory, Chl-a was extracted from filters using 10 mL of 90% acetone in the dark at 4°C for 24 h and quantified using a 10-AU Field Fluorometer (Turner Designs). The rest of the filters were freeze-dried and weighed to determine the SSC. The filter samples for POM were acidified with 2 N HCl to remove inorganic carbon, rinsed with Milli-Q water to wash off the retained acid, freeze-dried, and analyzed by an elemental analyzer coupled to an isotope ratio mass spectrometer (Flash 2000 and Delta V Plus; both from Thermo Fisher Scientific). International certified standards (USGS40, USGS43, USGS64, USGS73, and NIST8542) and certified soil standards (certificate number 341506; Thermo Fisher Scientific) were regularly used to calibrate the isotopic ratio and assess the precision, which was better than 0.2‰ for $\delta^{13}C_{POC}$, 2.3% for POC, and 5.5% for PN (1σ).

The concentration of nutrients was determined by colorimetric methods. Nitrite (NO_2^-) was evaluated according to the pink azo dye method (Strickland and Parsons, 1972). Nitrate (NO_3^-) was calculated by reducing nitrate to nitrite based on the cadmium-copper reduction method. The phosphate (PO_4^{3-}) and silicate (SiO_2) were derived by using the molybdenum blue method and silicon-molybdenum blue method (Murphy and Riley, 1962; Fanning and Pilson, 1973; Pai et al., 1993). Ammonia (NH_4^+) was evaluated *via* indophenol blue methods based on the Berthelot reaction (Ivančič and Degobbis, 1984; Aminot et al., 1997). CSK standards (Wako Pure Chemicals Ltd., Japan) and certified reference materials (KANSO Technos Co., Ltd., Japan) were used to calibrate every 10-15 samples. The precisions of the abovementioned methods were ±0.02 μmol L^{-1} for NO_2^-, ± 0.08 μmol L^{-1} for NO_3^-, ± 0.05 μmol L^{-1}, PO_4^{3-}, ± 0.1 μmol L^{-1} for SiO_2, ± 0.08 μmol L^{-1} for NH_4^+, respectively.

2.4 Surface sediment collection and analysis

Surface sediment samples were taken by a Shipek grab every 3 h for the grain-size analysis. The top 1~2 cm of the sediment in the grab bucket was collected into a plastic jar and stored in the refrigerator at 4 °C onboard. Then, sediments were freeze-dried in the laboratory. For grain-size frequency distribution analysis, 0.5 g sediment was treated by the following procedure: (1) washed with distilled water to remove the sea salt; (2) bathed with 10% hydrogen peroxide and hydrochloric acid for 24 h to dissolve organic materials and carbonates; (3) bathed with 1% sodium hexametaphosphate for 24 h and then shaken in the ultrasonic device for 30 sec to prevent aggregation; (4) measured by a laser diffraction size analyzer (LS 13 320, Beckman Coulter) to determine the particle-size distribution from 0.375 to 2,000 μm.

3 Calculations

3.1 Progressive vectors

The PV was derived based on the Lagrangian approach with the Eulerian measurement (*in-situ* flow field) and has been used in meteorology and marine physics (Liu et al., 2009; Su et al., 2015; Du and Liu, 2017; Ko et al., 2020). The PV was calculated as follows:

$$\overrightarrow{PV}_{X,z} = \sum_{t=1}^{m} \overrightarrow{X}_{z,t} + \overrightarrow{U}_{z,t} \times \Delta t)$$

$$\overrightarrow{PV}_{Y,z} = \sum_{t=1}^{m} \overrightarrow{Y}_{z,t} + \overrightarrow{V}_{z,t} \times \Delta t)$$

where X and Y indicate the east-west and north-south components of the PV, respectively; z is the water depth of the measured point; t is the time of the measurement; m is the sampling length; $\overrightarrow{X}_{z,t}$ ($\overrightarrow{Y}_{z,t}$) and $\overrightarrow{U}_{z,t}$ ($\overrightarrow{V}_{z,t}$) are the displacements and the velocities of the water parcel at the given time (t), respectively; Δt is the sampling interval. In this paper, only the horizontal PV displacements are shown because the measured vertical velocity on the mooring was unreliable.

3.2 Shear velocity

Using the Sedtrans05 model (Neumeier et al., 2008), shear velocities (u_*) induced by waves, currents, and current-wave interactions (marked as u_{*w}, u_{*c}, and u_{*cw}, respectively) were evaluated according to the bottom boundary layer theory. The input data included current speed, current direction, significant wave height, wave period, and wave direction. The first two parameters were recorded by the ADCPs; the rest were provided by the AQUAdopp (Figure 1B; Supplementary Table 1). The critical shear velocities (u_{*cr}) to resuspend particles of 63 and 153 μm sizes were calculated according to Van Rijn (1993). To estimate the possible range of the u_{*cr}, the assumed particle densities used in the calculation were 2.65 g cm^{-3} for the upper limit (quartz; detrital materials) and 1.5 g cm^{-3} for the lower limit (derived by the measured *in-situ* bulk density in this study), which is close to the value mentioned in Tian et al. (2022).

3.3 Spectral and coherence analyses

The frequency spectra and the coherence (the correlation between two spectra as the function of the frequency) among u_*, the light transmission, and VCs were computed to distinguish the process-response patterns in the resuspension process. The 'mscohere' functions in MATLAB were used and defined as follows (Welch, 1967; Rabiner and Gold, 1975; Kay, 1988):

$$S_{xx,f} = \frac{2\Delta t^2}{T} X_f X_f^* \quad ; \quad S_{yy,f} = \frac{2\Delta t^2}{T} Y_f Y_f^*$$

$$X_f = \text{fft}(x);\ Y_f = \text{fft}(y)$$

$$S_{xy,f} = \frac{2\Delta t^2}{T} X_f Y_f^*$$

$$C_{xy,f} = \frac{|S_{xy,f}|^2}{S_{xx,f} S_{yy,f}}$$

where $S_{xx,f}$ and $S_{yy,f}$ are the power spectra of the u_* and the light transmission (or VCs), respectively. Δt and T are the sampling period and the duration of the observation, respectively. X_f and Y_f are the results of the Fast Fourier Transform (FFT) for x and y. X_f^* (or Y_f^*) indicates the complex conjugate of the X_f (or Y_f). $S_{xy,f}$ is the cross power spectral density of x and y. $C_{xy,f}$ is the coherence between X_f and Y_f. All data were synchronized at 3 h intervals using linear interpolation before the analysis.

3.4 Particle bulk density

The particle bulk density (ρ_{bk}) is defined as the mass of the bulk particle (solid and void combined in a floc) divided by its total volume and expressed as follows (Hsu and Liu, 2010; Du et al., 2022):

$$\rho_{bk} = \rho_{IW} + (1 - \frac{\rho_{IW}}{\rho_p})(\frac{SSC}{VC})$$

Where the ρ_{IW} is the measured seawater density by CTD; ρ_p is the assumed density of the solid particle (2.65 g cm^{-3}); the SSC is the suspended sediment concentration measured by water filtration; the VC is the volume concentration measured by the LISST-100X (Supplementary Tables 1, 2). The low ρ_{bk} value indicates fluffy particles, such as flocs or biogenic particles, and vice versa (Lee et al., 2016; Du et al., 2022).

3.5 Marine fraction

To evaluate the terrestrial and marine proportions of POM in the bulk POC, a simple mixing model was used with the assumed $\delta^{13}C_{POC}$ end-member values at land and ocean to be -28.8‰ and -18‰, respectively (Goñi et al., 2000; Hu et al., 2006; Liu et al., 2006; Amiel and Cochran, 2008; Gireeshkumar et al., 2013; Lamb and Warn-Varnas, 2015; Ran and Zhang, 2015). The marine fraction (F_m) was subsequently defined as follows:

$$F_m(\%) = \frac{\delta^{13}C_{measured} - \delta^{13}C_{terrestrial}}{\delta^{13}C_{marine} - \delta^{13}C_{terrestrial}} \times 100$$

4 Results

4.1 Flow fields

The PV plot indicates that net flow movement was NE-ward with short-term tidal modulations with resolved M_2 and K_1 tides (our data was only long enough to resolve these two constituents; Figure 2; Lee et al., 2021). The current speed decreased from 0.39 m s^{-1} at 3 m to 0.12 m s^{-1} at 38 m (Supplementary Figure 2). The wind-driven flow field at the surface was mainly resulted from the *in-situ* wind (Zu et al., 2014; Chen et al., 2017; Lee et al., 2021). The bottom flow was caused by the upwelling-associated landward current along the Guangdong coast, which is controlled by the East Asian monsoon and the variation of the shelf topography (Gan and Allen, 2002; Gan et al., 2009b; Lee et al., 2021). To identify the signature of the water masses at the surface and bottom, the N/P ratio was superimposed on PVs as color-coded circles in Figure 2 for further discussion.

4.2 Water column structures

The T-S diagram and hydrographic profiles suggested at least two water masses were present at the study site. The upper water column shallower than 10 m was primarily occupied by the ZRP (Figure 3A), having a wide salinity range (28~32) and a narrow temperature span (28~31.5°C). Deeper than 10 m, the ambient

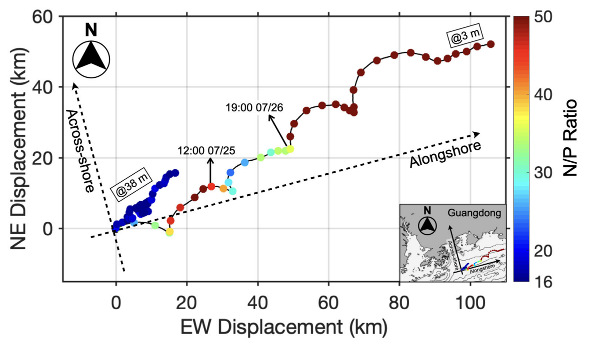

FIGURE 2
The progressive vectors (PVs) at the surface (3 m) and bottom (38 m). The N/P values (range indicated by the color bar to the right) are superimposed to indicate the sequential change of nutrient composition of the water mass. The marked time points indicate the duration having low N/P within the storm influence. The dashed arrows show the positive alongshore and across-shore directions. The PVs are plotted on a small-scale map (insert) to give a regional perspective.

coastal water had a very narrow salinity spread (33.5~34.7), and water temperature ranged from 21.5 to 29°C.

The water density (σ_t) structure showed a pronounced stratification from 18 kg m^{-3} at the surface to 24 kg m^{-3} at the bottom (Figure 3B). The light transmission and the fluorescence revealed a sandwich structure (Figures 3C, D). The light transmission was<50% at the surface, >80% in the middle of the water column, and<70% in the lower water column. The fluorescence was >1 μg L^{-1} at the surface, >0.5 μg L^{-1} at mid-depth, and<0.5 μg L^{-1} near the bottom.

In the upper water column, the temporal variability of all variables presented semi-diurnal to diurnal fluctuations, with the ZRP water having low water density, low light transmission, and high fluorescence (Figure 3B–D). The fluctuation was suppressed around 18:00 07/26 when the surface water had higher water density, higher light transmission, and lower fluorescence. At mid-depth, there was a noticeable layer of high fluorescence around the depth of 22 m, having a thickness of about 5 m in which the fluorescence was consistently higher (>0.5 μg L^{-1}). This has been reported as the subsurface chlorophyll maximum (SCM) in the NSCS (Lu et al., 2010; Chen and Zhao, 2021). A similar fluorescence/Chl-a subsurface maximum layer was also found in the Taiwan Strait and associated with the intermediate nepheloid layer (INL; Du and Liu, 2017; Liu et al., 2019). The SCM corresponding to the relatively high but low light transmission in the mid-depth layer (80~85%; Figures 3C, D) suggests the phytoplanktonic nature of SPs at this depth (Du and Liu, 2017). In the bottom water mass, the water density and fluorescence were consistent at 24 kg m^{-3} and 0.25 μg L^{-1}, respectively (Figures 3B–D). However, the light transmission at this depth revealed a semi-diurnal to diurnal variability, ranging between 60% and 70%.

4.3 Nutrients and Chl-a

Nutrients were measured to constrain the interpretation of the water mass (Figure 4). The silicate changed from 0.99 to 6.10 μmol L^{-1} at the surface and from 6.86 to 11.01 μmol L^{-1} at the bottom (Figure 4A). The concentration of the Chl-a ranged from 0.3 to 2.5 μg L^{-1} at the surface but was nearly constant at the bottom (~0.3 μg/l; Figure 4B). The concentration of total N (sum of nitrate, nitrite, and ammonia) ranged from 0.85 to 4.86 μmol L^{-1} at the surface and from 4.94 to 8.28 μmol L^{-1} at the bottom (Figure 4C). The phosphate changed between below detection and 0.1 μmol L^{-1} at the surface and varied between 0.31 and 0.55 μmol L^{-1} at the bottom (Figure 4D). Although nutrients and Chl-a did not exhibit a clear trend at the surface, most parameters increased at the bottom in the 5-day observation, noticeably in the silicate (Figures 4A-D; Supplementary Figure 3).

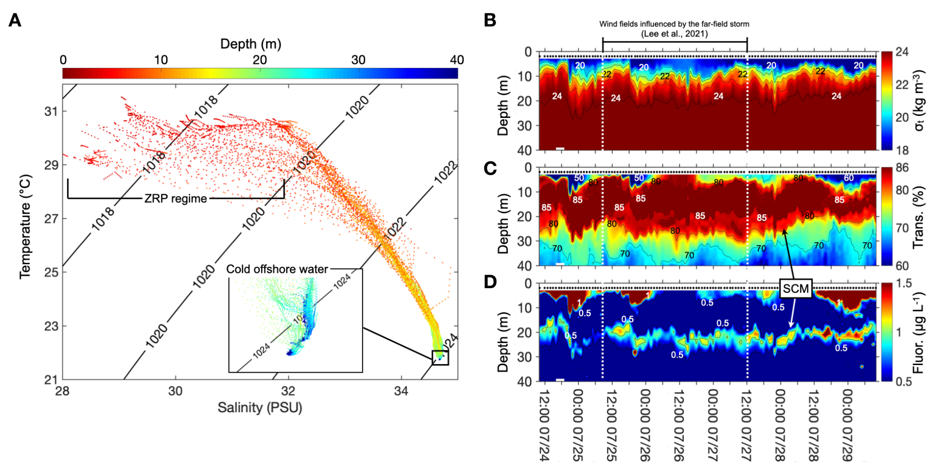

FIGURE 3
Hydrographic measurements at ZHJ2 including **(A)** The depth-referenced T-S diagram in which the color bar indicates the depth of the measurement. Warm colors represent shallower depths and cold colors represent deeper depths. The inserted graph is the enlarged section of the T-S diagram at the bottom marked by the black square. The temporal changes in 2-D structures are shown in **(B)** the water density, **(C)** the light transmission, and **(D)** the fluorescence. White dash lines in **(B-D)** mark the duration of the storm influence. Arrows point out the SCM.

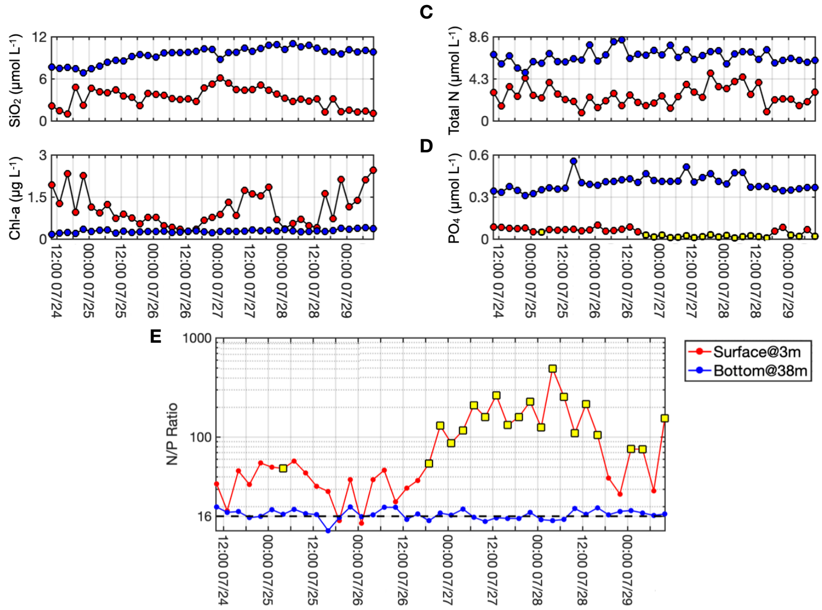

FIGURE 4
Temporal variabilities of **(A)** silicate, **(B)** Chl-a, **(C)** total N (nitrate + nitrite + ammonia), and **(D)** phosphate, and **(E)** the N/P ratio at the surface (red dots and line) and bottom (blue dots and line) at ZHJ2. The black dashed line in **(E)** indicates the Redfield ratio. The yellow squares marked data points of phosphate concentration below the detection limit.

The N/P ratio at the surface covered a wide range between 13.5 and 491.5 (Figure 4E). The average value was 96, which was six times greater than the Redfield ratio (N/P = 16; Yin et al., 2001). The N/P ratio at the bottom was much lower than that at the surface and ranged between 11.4 and 19.9. Although the concentration of nutrients at the bottom increased (Supplementary Figure 3), the N/P ratio was consistent around the Redfield ratio (Figure 4E).

4.4 Physical properties of suspended particles

The VC of<63 and 63-153 μm size classes were abundant in the upper water column (>4 μL L^{-1}) and near the bottom (1~2 μL L^{-1}; Figures 5A, B). The VC structure of the >153 μm showed higher values in water depth shallower than 25 m with a range from 10 to >50 μL L^{-1} and significantly decreased to<5 μL L^{-1} in the lower water column (Figure 5C). VCs at the surface presented semi-diurnal to diurnal fluctuations that were suppressed at around 18:00 07/26 (Figures 5A–C), which was consistent with the CTD profile. The corresponding parameters of the VC (such as light transmission and fluorescence) indicated the influence of the ZRP at the surface and the turbid water at the bottom (Figures 3C, D, 5A–C). Although the depths shown in the VC might deviate, the correspondence among variables suggests that large particles (>153 μm) trapped in the middle of the water column resulted from the stratification (Figure 3B, 5C). Similar VC structures are also observed in the river plume regime seaward of the mouth of the Minjiang River (Du and Liu, 2017).

The temporal distribution of VCs showed size-fractionated structures in the upper water column. At the surface, the VC of<153 μm increased as the salinity decreased (Figures 5A, B; Supplementary Figure 4). However, particles in the >153 μm size class had a higher VC at the salinity peak, known as the plume front, where there was mixing between ZRP and ambient sea waters (Figure 5C; Supplementary Figure 4; Garvine and Monk, 1974; Lee et al., 2016; Li et al., 2021). The VC composition indicates the coarsest particles of >153 μm contributed the most to the total VCs at the surface with an average of 65% and a maximum of 94% (Figure 5D), and the<63 m size class was the second most abundant with an average of 26%. The two smallest size classes were minor in the upper water column but dominant at the bottom, with<63 μm having an average of 50% in the VC composition (Figure 5E). To compare the size composition of the bulk SSC with VCs, the SSC was divided into<63 μm, 63-153 μm, and >153 μm size classes (Figures 5F, G). The average SSC at the surface was 4.6 mg L^{-1} with a maximum of 19.6 mg L^{-1} (Figure 5F). In the bottom water, the average SSC was 5.4 mg L^{-1} with a maximum of 19.7 mg L^{-1} (Figure 5G). The<63 μm size class contributed most to the bulk SSC both at the surface and near the bottom, and the >153 μm size only contributed lower than 30%. Based on the measured VCs and SSCs, the particle bulk densities (ρ_{bk}) at the surface ranged between 1.03 and 1.52 g cm^{-3} and averaged 1.19 g cm^{-3} (Supplementary Figure 5). The ρ_{bk} ranged between 1.21 and 2.48 g cm^{-3} and averaged 1.51 g/cm^3 at the bottom. It is worth mentioning that the range of ρ_{bk} is influenced by the assumed density of the solid particle, which is related to the *in-situ* composition of the SP.

4.5 Chemical characteristics of suspended particles

The bulk POC ranged from 0.06 to 0.19 mg L^{-1} at the surface, and 0.05 to 0.08 mg L^{-1} at the bottom (Figure 6A). The POC% in the

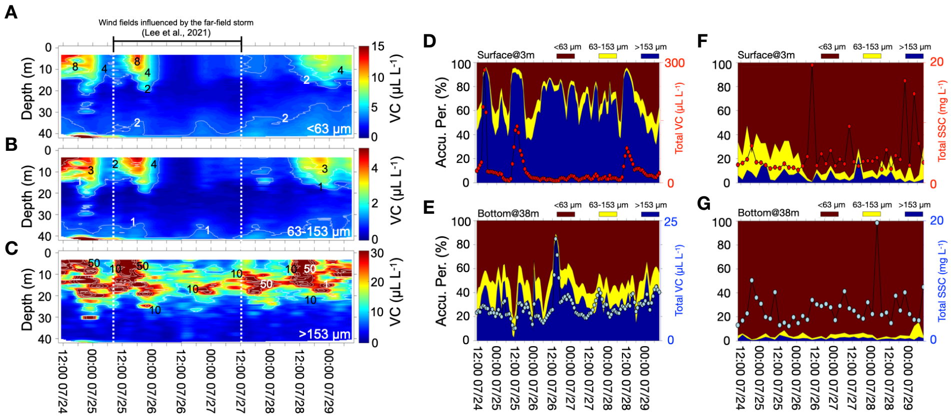

FIGURE 5
Temporal changes of the 2-D structure of the volume concentration (VC) of the size of **(A)** <63, **(B)** 63-153, and **(C)** >153 μm. The white dash lines in **(A-C)** mark the duration of the storm influence. Temporal variabilities of the accumulative percentages of size compositions of VC and SSC at the surface **(D, F)** and the bottom **(E, G)**. The color codes above each frame indicate different size classes.

total SSC varied between 1.05 and 7.09% at the surface and 0.57 and 2.85% at the bottom (Figure 6B). The bulk PN at the surface water varied from 0.01 to 0.03 mg L^{-1}, of which PN% in the total SSC varied between 0.16 and 1.04% (Figures 6C, D). In the bottom water, the bulk PN ranged between 0 and ~0.01 mg L^{-1}, with PN% from 0.06 and 0.29%. Overall, the concentration of POC and PN decreased when the salinity increased in the surface water but rarely changed in the bottom water (Figures 6A, C). The decrease of POC % and PN% with increasing SSC can be fitted with the power regression ($R^2 > 0.6$; Figures 6B, D). Guo et al. (2015) also observed similar results in the Zhujiang estuary and ascribed the pattern to the dilution of organic matter by clastic materials.

The POC to the Chl-a ratio (PC ratio) was used to identify the degradation of the POM (Figure 6E; Wang et al., 2011; Guo et al., 2015). The threshold of the PC ratio between the newly produced phytoplankton and the degraded materials (or detrital) is 200. If the PC ratio is lower than 200, the newly grown phytoplankton dominates and vice versa. Our results show that most PC ratios at the surface were lower than 200 in general (the value changed from 57.7 to 327.3) with a wide range of Chl-a values. The bottom POM showed PC ratios close to or higher than 200 (from 156.5 to 462.5) with a narrower range of Chl-a.

The atomic carbon-to-nitrogen ratio (C/N ratio) ranged from 6.17 to 8.31 at the surface, having an average of 7.4 and a standard deviation of 0.52; it ranged from 5.89 to 19.19 at the bottom, having an average of 10.7 and a standard deviation of 2.71 (Figure 6F; Supplementary Figure 6). The surface $\delta^{13}C_{POC}$ varied from -25.38 to -18.93‰, with a mean value of -21.76‰ and a standard deviation

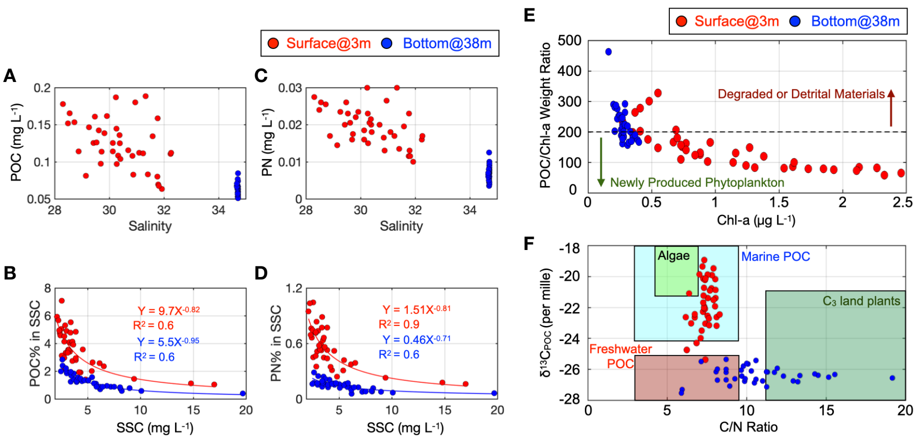

FIGURE 6
Measured OM parameters from water samples taken at the 3 (red) and 38 m (blue) depths, respectively. **(A)** The concentration of POC vs. salinity, **(B)** the POC% is plotted against the SSC with power regression lines, R^2, and the fitting equations. **(C)** The concentration of PN vs. salinity, **(D)** the PN % is plotted against the SSC with the power regression lines, R^2, and the fitting equations. **(E)** The POC to Chl-a ratio vs. measured Chl-a at the surface (red dots) and bottom (blue dots). The black dashed line indicates the demarcation value at 200. **(F)** The $\delta^{13}C_{POC}$ vs. C/N diagram. Boxes indicate the different domains of OM in the C/N vs. $\delta^{13}C_{POC}$ diagram (data compiled from Bordovskiy, 1965; Haines, 1976; Sherr, 1982; Schidlowski et al., 1983; Meyers, 1994; Peterson et al., 1994; Middelburg and Nieuwenhuize, 1998; Chivas et al., 2001; Raymond and Bauer, 2001; Cloern et al., 2002; Lamb et al., 2006; and references therein).

of 1.53‰. The bottom $\delta^{13}C_{POC}$ ranged between -27.55 and -25.35‰ with an average of -26.37‰ and a standard deviation of 0.51‰. According to the C/N ratio and the $\delta^{13}C_{POC}$, the signature of the POM is characterized as marine sourced at the surface (enriched $\delta^{13}C_{POC}$) but terrestrial sourced at the bottom (depleted $\delta^{13}C_{POC}$).

The F_m showed that the proportion of the marine POM ranged between 31.7 and 91.4% at the surface (Figure 7), and the average value was 65.2%. The F_m increased when the salinity decreased, and vice versa. This indicates that the marine POM was dominant in the river plume regime. The F_m in the bottom layer was much lower than that at the surface and was constant around the value of 22.5%, which implies low marine POM content.

4.6 Surface sediment

The grain-size composition of the surface sediment was slightly bimodal (Figure 8A). One peak was at 12 µm, and the other was at 60 µm. Following the previous convention (Lee et al., 2016; Du and Liu, 2017; Du et al., 2022; Liu J. T. et al., 2018), the size classes were classified into<63, 63-153, and>153 µm for cross-comparison with other measured variables (Figure 8B). Most of the contribution (84%) to the bulk volume in the surface sediment was from the<63 µm grain-size class. The second most contribution (15%) was from the 63-153 µm grain-size class. The >153 µm grain size class only contributed<1% to the bulk volume.

4.7 Shear velocity

The u_{*c} ranged from 0.1 to 10.8 mm s^{-1} and varied semi-diurnally to diurnally (Figure 9). Because of the comparatively low significant wave height (< 1.5 m on average; Supplementary Figure 1), the derived u_{*w} was close to 0 mm s^{-1}. Thus, the u_{*cw} was mainly affected by the flow field and followed the variability of the u_{*c}. To clarify the process-response of the resuspension, u_{*cr} in the 63 µm grain-size class ($u_{*cr\_63\mu m}$) was calculated with the particle densities having 2.65 g cm^{-3} (detrital material; $u_{*cr\_63\ detrital}$; red line) and 1.5 g cm^{-3} (*in-situ* particle bulk density near the bottom in Supplementary Figure 5; $u_{*cr\_63\ in\text{-}situ}$; red dashed line). Although u_{*cw} rarely exceeded the entrainment threshold for detrital material of 63 µm ($u_{*cr\_63\ detrital}$ at 9.1 mm s^{-1}), it was beyond the $u_{*cr_{63\ in\text{-}situ}}$ at 5.5 mm s^{-1} frequently (Figure 9). However, the u_{*cw} was still lower than $u_{*cr\_153\mu m}$ in both cases (detrital material and *in-situ* bulk density) at 17.2 mm s^{-1} and 8.3 mm s^{-1}, respectively.

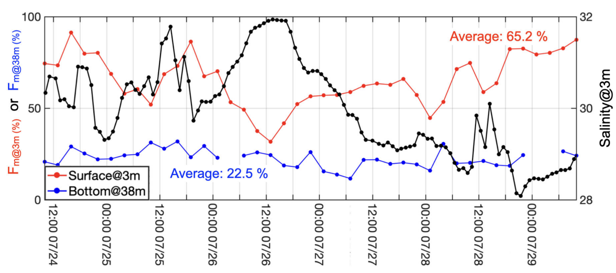

FIGURE 7
The derived F_m at 3 and 38 m (marked with red and blue lines, respectively). The black line indicates the salinity measured at 3 m during the observation.

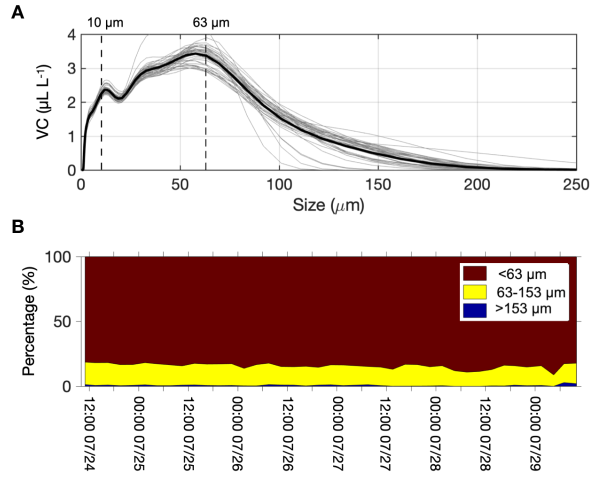

FIGURE 8
The grain-size composition of the surface sediments collected at ZHJ2 including **(A)** the size distribution in VC of all samples; **(B)** temporal changes in percentage of size composition in VC.

4.8 Frequency spectral and coherence analysis

The frequency spectrum of the shear velocity showed an intense energy peak centered at the diurnal frequency (Figure 10A). Similar patterns were also found in the light transmission and VCs within 1.5 mab, except for the >153 µm grain-size class that showed higher energy at 0.8 cycles per day (Figure 10B–E). The power density of the VC in the<63 µm size class was more substantial and more concentrated at the diurnal frequency than that in other size classes.

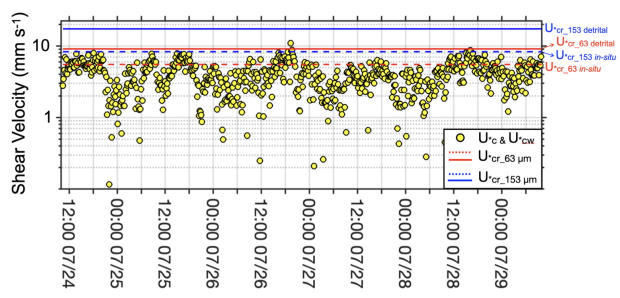

FIGURE 9
Calculated shear velocities induced by currents and current-wave couplings (u_{*c} and u_{*cw}, marked with yellow dots). The dashed and solid red lines indicate the critical shear velocities of the 63 µm grain size with the measured particle density (1.53 g cm^{-3}) and the assumed detrital density (2.65 g cm^{-3}), respectively. The dashed blue and solid lines indicate the critical shear velocities of the 153 µm grain size with the measured particle density and the assumed detrital density, respectively.

Among the three sizes, the 63-153 μm class was able to be entrained the highest above the seabed (up to 1.5 m). The spectral coherence of the shear velocity to the light transmission and VCs revealed a high peak (>0.7) at the diurnal period, except for the coarsest size class in the VC (Figure 10F–I).

5 Discussion

5.1 The ZPR regime and SPs dynamics in the upper water column

Previous studies have described that the mechanisms controlling the dispersion of the ZRP are couplings among the wind field, tidal and non-tidal flows, and upwelling currents (Zu et al., 2014; Zu and Gan, 2015; Lee et al., 2021). The southwesterly monsoon wind field dominates in the summer and drives the less saline ZRP water northeastward along the Guangdong coast (Figure 2; Gan et al., 2009a; Zu and Gan, 2015; Lee et al., 2021). The diluted ZRP water mass occupies the upper water column of the NSCS and carries abundant Zhujiang effluent. Therefore, the surface water displayed the signature of low water density, low light transmission, high fluorescence, and high VCs on the pathway of the ZRP (referred to as the ZRP regime; Figure 3, 5A–C).

The high N/P ratio at the surface in the NSCS is considered the signature of the ZRP water (Figures 2; 4E; Yin et al., 2001), which was caused by the excessive N exported from the Zhujiang River due to the fast-growing population and agricultural industries along the upper reaches (Yin et al., 2001). Phytoplankton growth was stimulated when the ZRP delivered high riverine N to the N-limited NSCS (Huang et al., 2020). Our data shows that the POM in the ZRP regime was marine-sourced and "fresh" (growing *in-situ* or in the adjacent area) instead of exported riverine algae (Figures 6E, F; Supplementary Figure 6A). Although POC only contributed 4% to the bulk SSC on average at the surface (Figure 6B), this value is comparable to those in the Changjiang River and Rhône River (Lorthiois et al., 2012; Zhao and Gao, 2019). The maximum proportion of those marine POM reached 90% in the ZRP regime which varied independently against the salinity (Figure 7). The particle size also changed against the salinity, which had finer SPs (<153 μm) in the ZRP regime but coarser size class (>153 μm) at the plume front (Figure 5A-C; Supplementary Figure 4). The bulk density of the SP (1.19 ± 0.13 g cm^{-3}) indicates that particles at the surface water were fluffy with low mass, such as phytoplankton or flocs (Figure 6F; Supplementary Figure 5; Gregory, 1998; Lee et al., 2016; Du et al., 2022).

5.2 The coupling between physical processes and the particle biogeochemistry at the surface

Because of the co-varying nature of the data that included physical forcing, water mass property and the nature of particles, a multivariate analysis technique, empirical orthogonal function (EOF) analysis, was used to render interpretations on the inter-relationship among all variables (Liu et al., 2019; Liu et al., 2021; Yang et al., 2021; Du et al., 2022). The covariability of several independently measured variables at 3 m were synchronized at 3-hr intervals to be objectively deciphered by each eigenmode (Figures 11, 12). In the analysis, the measured flow field was decomposed into alongshore and across-shore components. Then the non-tidal and tidal parts of each alongshore and across-shore flow were separated. The non-tidal flow represents the wind-driven

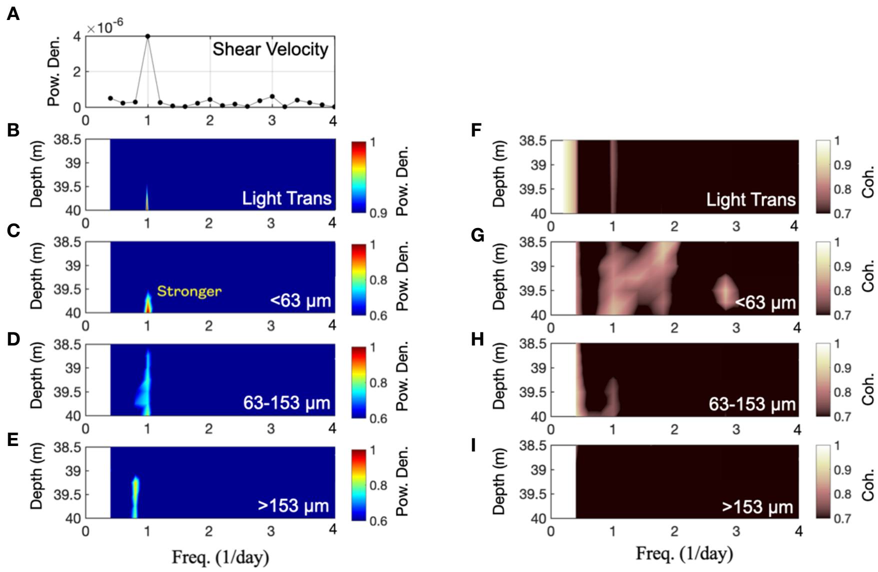

FIGURE 10
Power spectra and coherence plots of **(A)** the shear velocity (u_{*cw}); **(B-E)** light transmission, and VCs in<63, 63-153, and >153 μm grain size classes, respectively in the depth range of 38.5~40 m; **(F-I)** The coherence between the spectra of the light transmission and VCs in<63, 63-153, and >153 μm grain size classes, respectively in the depth range of 38.5~40 m.

flow. The tidal flow represents tidal motions. The salinity, temperature, and light transmission stand for the signature of the water mass. A Static Stability Index (E value), which has been used to quantify the water column stability (Du and Liu, 2017; Lee et al., 2021), was included to represent the mixing processes. The PC ratio and F_m indicate the biogeochemical properties of the SP related to its transformation (newly produced or degraded) and source/provenance (marine or non-marine). The ρ_{bk} represents the physical property of the SP. The variables with higher values of eigenvectors are the dominant variables influencing the co-variability of a particular eigenmode (Figures 11, 12). The interpretation of EOF results is subject to the user's experience and knowledge of the analyzed variables (Liu et al., 2019).

At the surface, the first three eigenmodes of the EOF analysis explained 64% of the standardized covariance in the original dataset (Figure 11A–C). In the 1st eigenmode (31%; Figure 11A), the eigenvectors in the positive group included landward non-tidal flow (representing physical forcing), salinity, temperature, light transmission (representing offshore water), PC ratio (representing degraded materials), and ρ_{bk} (representing denser texture). The negative group included E value and F_m (representing low water stability and depleted $\delta^{13}C_{POC}$). These groupings indicated the landward non-tidal flow that delivered the offshore water mass of higher salinity, temperature, and light transmission (lower turbidity), which was opposite to the water column stability. Furthermore, the landward transport of offshore water entrained more depleted $\delta^{13}C_{POC}$ and degraded particles having a high bulk density.

The temporal pattern of the 1st mode grouping is represented by the eigenweighting curve, plotted against selected variables for comparison (Figure 11D). The variables that mimic the eigenweighting curve of this mode are non-tidal across-shore flow and salinity; and the E and F_m curves are the mirror images of the eigenweighting curve. The zero-crossings of the eigenweighting curve indicate the time that the landward non-tidal flow occurred under the influence of the far-field storm wind and suggests the regime shift at the surface (Figure 11D; Huang et al., 2020; Lee et al., 2021). The low surface N/P ratio in the same period was attributed to the strong wind-induced mixing (low E) between the ZRP and ambient waters (Figure 2; Supplementary Figure 7). The out-of-phase relation of the F_m to the eigenweighting curve suggests that more depleted $\delta^{13}C_{POC}$, degraded, and denser POM became dominant when the surface was filled with offshore water (Figures 7, 11A, D). Therefore, the 1st mode described the influence of the far-field wind forcing on regimes in the upper water column.

The eigenvectors in the 2nd mode (21%) showed dominance by tidal motions in both alongshore and across-shore directions (Figure 11B). The eigenweighting curve presented in phase with the flood tide (NE-directed alongshore and the inshore-directed across-shore tidal flows; Figure 11E) and out of phase with salinity. Therefore, this mode indicates the on/off-shore dispersal of the ZRP by the tidal modulation (Lee et al., 2021). During the flood tide, the warm river plume enhanced the stratification in the upper water column (positive temperature, negative salinity, and positive E in eigenvectors; Figures 11B, E) and had less turbidity (high light transmission), with fresh marine-sourced POM (negative PC ratio and positive F_m);. When the ebb tide pushed the ZRP offshore, the regime at the surface shifted to the turbid plume front which contained more degraded POM having a denser ρ_{bk} and the less enriched-$\delta^{13}C_{POC}$ (Figure 11B; Supplementary Table 3).

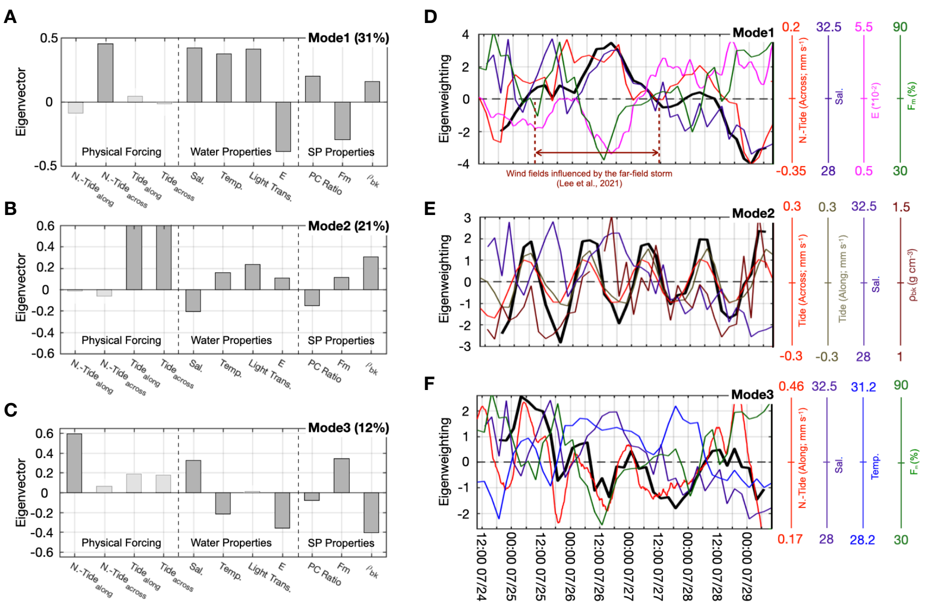

FIGURE 11
Plots of the EOF analysis results including **(A-C)** Eigenvectors of the first three modes. The dominant variables are in dark gray, and the rest are in light gray. The eigenweighting curve of each mode (bold black curve) is potted against the selected variables including **(D)** the across-shore non-tidal flow (red), salinity (dark purple), E (magenta), and F_m (green); **(E)** the across-shore tidal flow (red), the alongshore tidal flow (yellow-green), salinity (dark purple), and particle bulk density (brown); **(F)** the along-shore non-tidal flow (red), salinity (dark purple), water temperature (blue), and F_m (green). The duration influenced by the storm wind is marked with the brown dashed lines in **(A)**.

The eigenvectors in the 3rd mode (12%) show the dominant variables in the positive group were the alongshore non-tidal flow, the salinity, and the F_m (Figure 11C). The dominant negative variables included the water temperature, E, PC ratio, and ρ_{bk}. These groupings indicated the NE-ward non-tidal flow was associated with the transport of the saline and cold-water mass that carried newly produced and marine-sourced particles with low ρ_{bk} at the surface. Since Wang et al. (2014) pointed out that the strength of the NE-ward flow had a recognizable contribution to the upwelling intensity in the NSCS, this mode infers the effect of the varying upwelling. The secular trend of the eigenweighting curve was accompanied by the decreasing non-tidal alongshore flow and salinity, implying the regime shifted from the saline upwelling regime to the ZRP regime during observation (Figure 11F), which was observed by the SST satellite images (Supplementary Figure 8; Multiscale Ultrahigh Resolution SST product; JPL MUR MEaSUREs Project, 2015). The corresponding biogeochemical properties of SPs, such as $\delta^{13}C_{POC}$-derived F_m and ρ_{bk}, changed due to different bio-communities in the ZRP and upwelling regimes (Yin et al., 2001; Li et al., 2021). Our results showed that POM in the upwelling regime carried lighter biogenic particles having more enriched $\delta^{13}C_{POC}$ than that in the ZRP regime (Figure 11C; Supplementary Table 3; Gan et al., 2010; Lu et al., 2010; Gao et al., 2018).

5.3 The BNL regime and SPs dynamics near the bottom

The bottom regime was identified by the presence of a 10-m thick benthic nepheloid layer (BNL), which is characterized as the water mass with low light transmission than that in the ambient seawater (Figure 3C; Hoshika et al., 2003; Du and Liu, 2017; Tian et al., 2022). The average light transmission in the BNL (68%) was comparable to that in the surface ZRP (71%). Although the BNL has been widely observed in estuaries and marginal seas (Liu et al., 2014; Du and Liu, 2017; Jia et al., 2019; Feng et al., 2021), studies of particle dynamics in the BNL on the NSCS shelf are still in progress (Gong et al., 2020; Li et al., 2021).

The high bulk density of particles and PC ratio in the bottom regime indicated that the POM was degraded (Figures 6; Supplementary Figure 5). This resulted in a low proportion of bulk SP (<3% in POC and<0.3% in PN) and a wide range of C/N ratios with a weak linear relationship (R^2<0.12) between the atomic carbon and nitrogen (Figure 6F; Supplementary Figure 6B). The degraded POM in the BNL was suggested as "terrestrial-sourced" due to the depleted $\delta^{13}C_{POC}$ values (lower/lighter than -25‰; Figure 6F), which could be caused by the microbial effects or degradation (Liu et al., 2007; Close and Henderson, 2020). The F_m indicated that the proportion of marine materials (enriched $\delta^{13}C_{POC}$) only contributed 22.5% of the bulk POM in the bottom regime (Figure 7). Interestingly, there is a missing link to interpret the source of the $\delta^{13}C_{POC}$ in the BNL because both the ZRP and previous surface sediment records had enriched $\delta^{13}C_{POC}$ in the bulk POM (Yu et al., 2010; Guo et al., 2015; Cao et al., 2020). Therefore, the EOF analysis was used to determine the complex process-response relationship between the physical forcing and SPs in the bottom regime.

5.4 The coupling between physical processes and particle biogeochemistry near the bottom

In the EOF analysis (Figure 12A), the PVs of non-tidal flows (Supplementary Figure 2D; Lee et al., 2021) were chosen to represent the net movement/displacement of the bottom water mass as part of the upwelling-associated circulation and were divided into along-shore and across-shore components. The tidal flow represented the tidal forcing. The salinity, temperature, and light transmission represented the bottom water mass. PC ratio, F_m, and VCs represented properties of SPs. VCs were separated into two groups using the 63 μm as the bench line to represent the responses in SPs of different sizes under various hydrodynamic forcing. Only the first two eigenmodes (accounting for 56% of the data) are described in the following section because the third mode only explained<10% of the standardized covariance of the original dataset.

The 1st eigenmode explains 42% of the standardized covariance (Figure 12A). Based on the eigenvectors, the positive PVs in both components represent the net NE-alongshore and landward movements of water masses having low salinity, low temperature, and low light transmission (variables in the negative group). The POM carried by the water masses was degraded and depleted-$\delta^{13}C_{POC}$ (positive PC ratio and negative F_m) and dominated by finer particles partially with coarser size (highly positive in $VC_{<63\mu m}$ and less in $VC_{>63\mu m}$). The eigenweighting curve in the first mode having an increasing secular trend illustrates the main biogeochemical attributes of the SPs associated with the intrusion of the cold offshore water driven by the upwelling circulation (Figures 2, 12C; Supplementary Table 4; Lee et al., 2021).

The 2nd mode explains 14% of the covariability showing the dominance of tidal forcing (Figure 12B). The combined SE tidal flow (positive in the alongshore tidal flow and negative in the across-shore tidal flow) caused the bottom water to become more turbid (negative light transmission), and the POM were degraded, marine-sourced, and finer materials (positive PC ratio, F_m, and $VC_{<63\mu m}$).

The 2nd mode eigenweighting curve presented a semidiurnal to diurnal variability and mimicked the variability of the tidal flow (Figure 12D). Since the power density spectrum of the shear stress, the light transmission, and VCs showed pronounced peaks located at/near the diurnal frequency with high coherences (Figure 10), a forcing-response relationship in the entrainment of bottom sediment caused by the tide-related process is clear. The resolved tidal flows near the bottom were likely to generate turbulences inducing resuspension of particles having high bulk density (Supplementary Figure 5; Lee et al., 2021; Liu J. T. et al., 2018; Weeks et al., 1993). The eigenvector of the $VC_{>63\mu m}$ was negative (Figure 12B) because the theoretical entrainment analysis based on the bulk density of particles indicated the strength of the u_{*cw} was

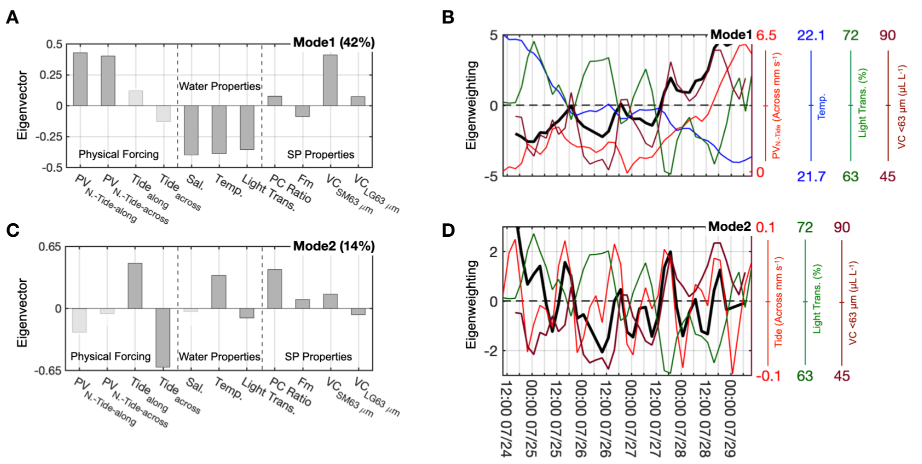

FIGURE 12
Plots of the EOF analysis of results. **(A, B)** Eigenvectors of the first two modes. The dominant variables are in dark gray, and the rest are in light gray. The eigenweighting curve of each mode (bold black curve) is potted against the selected variables including **(C)** the across-shore non-tidal PV (red curve), temperature (blue), light transmission (green), and VCs in the <63 μm size class (brown); **(D)** the across-shore tidal flow (red), light transmission (green), and VCs in the<63 μm size class (brown).

insufficient to suspend coarser particles (Figure 9). This explains why the high coherence to the shear velocity only occurred in the VCs of finer size classes at the diurnal frequency (<153 μm; Figures 10G–I). In addition, the surface sediment was mainly composed of<153 μm, which limited the "source" of coarser particles to be suspended (Figure 8, Supplementary Table 4).

5.5 Contrasting regimes in the water column

Although both wind field and tidal forcing played important roles at surface and bottom regimes, the processes-responses were different in the physical forcing and biogeochemical properties of SPs (Figures 11 – 13). At the surface, the summer monsoon wind and tidal flows resulted in the coastal circulations that controlled the dispersal of the regime among upwelling, plume front, and ZRP (Figures 13A, B, E, F). With the episodic far-field storm wind, the mixing processes among regimes increased (Figure 13D). Near the bottom, on the other hand, the southwesterly monsoon wind field was associated with the landward transport of the cold offshore water through the upwelling circulation (Figure 13B). The tidal oscillation caused the local sediment resuspension off the seabed, which led to the development of the BNL (Figures 13B, C)

The corresponding POM in surface regimes was newly produced marine phytoplankton because the ZRP and upwelling delivered nutrients supporting the primary production (Figure 13B). In the lower water column, by contrast, the degraded POM was attributed to the particles entrained from the offshore and reworked surface sediments (Figures 13B, C). Therefore, the biogeochemical properties of the SP exhibited lighter particle bulk density and more enriched $\delta^{13}C_{POC}$ at the surface (fluffy biogenic particles) than those in the lower water column (denser detrital materials having a depleted $\delta^{13}C_{POC}$; Figures 6E, F; Supplementary Figure 5).

The SPs showed size-fractionated nature in the water column, that there are coarser particles (>63 μm) at the surface but finer particles (<63 μm) at the bottom (Figures 5D, E). Regimes at the surface had diverse particle sizes among ZRP (<153 μm), the plume front (>153 μm), and the upwelling region (20-200 μm; Li et al., 2021), which was caused by the different bio-growing mechanisms and the mixing processes (Figures 5A-C; Supplementary Figure 4; Lee et al., 2016; Li et al., 2021). Furthermore, large particles were trapped below the pycnocline due to stratification caused by the ZRP (Figure 3B, 5C; Du and Liu, 2017; Liu et al., 2019).

5.6 Implications on the close coupling between physics and particle-related biogeochemistry on river-dominated continental shelves

Satellite images, *in-situ* observations, and numerical modeling have suggested the effluent exported from the Zhujiang is transported to the southern Taiwan Strait in summer (Chen, 2002; Gan et al., 2009b; Bai et al., 2015; Lee et al., 2021). However, our field measurements demonstrate that ZRP mainly consisted of marine-sourced POM instead of terrestrial POM (Figure 6). A similar POM composition was also found in the plumes of the Changjiang River (Gao et al., 2014) and the Amazon River (Weber et al., 2017), but not in the case of abundant riverine C3 sources in the Rhône River and Fly River (Goni et al., 2006; Harmelin-Vivien et al., 2010). The different source identification of SPs affects the evaluation of the OM budget on the pathway of ZRP. With the proportion of marine OM and the derived bulk density of SPs in the water column (Figure 7, Supplementary Figure 5), the transport and settling flux of OM can be precisely estimated on the inner shelf of the NSCS.

The EOF analysis provides a powerful tool to objectively differentiate the effects of non-tidal and tidal forcing on the

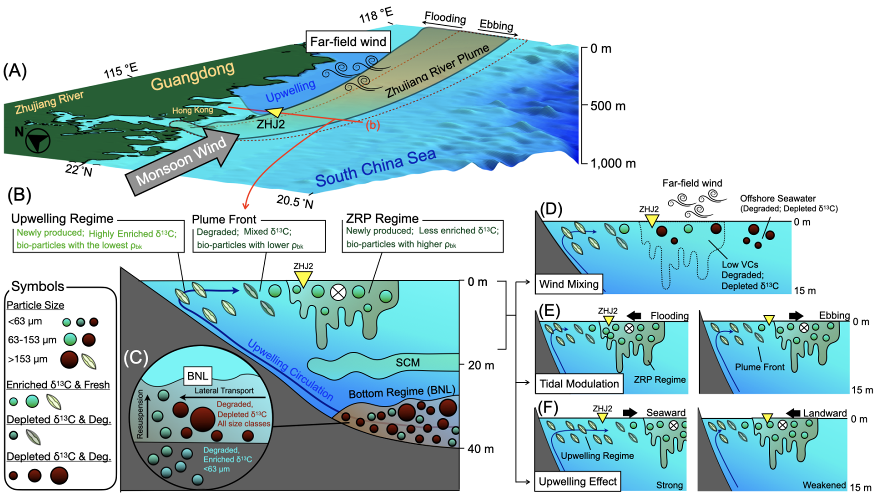

FIGURE 13
A schematic diagram illustrating process-response relationships among the physical forcing and types of SPs, including **(A)** The bird's view of the physical forcing includes the southwesterly monsoon wind, tidal modulations, and far-field wind along the propagation pathway of the ZRP. **(B)** Along the transect in **(A)** shows regimes entraining SPs in the water column (the transect in **(A)** is marked "**(B)**"). The characteristic of each regime is described in the box above the **(B)**. Different symbols on the left indicate the types of particles. **(C)** The circle shows an enlarged BNL. The cause-and-effectiveness between the physical forcing and SPs in the upper water column is on the right, such as **(D)** the mixing induced by the far field wind, **(E)** the tidal modulations, and **(F)** the upwelling-associated effect. The inverted yellow triangle indicates the location of ZHJ2. .

associated water masses and diverse sources of particles in the sediment transport process. For example, the discrepancy in $\delta^{13}C_{POC}$ between the bottom water mass (-26.37‰) and the surface sediment (-24‰ ~ -23‰) has been observed on the inner continental shelf of the NSCS (Yu et al., 2010; Guo et al., 2015; Cao et al., 2020), but the cause-and-effect is challenging to validate due to the complicated coupling of physical forcing. The EOF analysis demonstrates that the upwelling-associated landward transport delivered the degraded POM having depleted $\delta^{13}C_{POC}$ to the nearshore, while the tide-related forcing entrains enriched $\delta^{13}C_{POC}$ particles from sediment. The combination of physical processes resulted in a depletion of the overall $\delta^{13}C_{POC}$ in the BNL. Without constraints of physical forcing, identifying the particle source based only on the biogeochemical properties of the SP might be misleading. Understanding the process-response nature of SPs in the upwelling-favorable environments helps to establish the source-to-sink (S2S) conceptual framework for biogeochemical cycles on the river-dominated continental shelf like the NSCS.

6 Conclusion

This study used an interdisciplinary approach to investigate the close coupling between physical processes and biogeochemical properties of SPs on the pathway of the ZRP in the NSCS. Although the water depth was only 41 m at our study site, distinct oceanographic regimes were present at the surface and bottom due to different physical forcing, including the wind field, coastal currents, tidal oscillations, and upwelling. (Figure 13). Water masses in the surface regime included cold upwelling water and the warm ZRP, with the plume front having mixed water mass in between. The dispersal of the ZRP was controlled by the monsoon wind, wind-driven currents, and tidal flows. The newly produced marine-sourced POM (enriched $\delta^{13}C_{POC}$) was generally observed in the surface. However, due to different bio-communities in the surface regime, the ZRP contained smaller particles (<153 μm) with higher bulk density and less enriched $\delta^{13}C_{POC}$. At the plume front, the POM was degraded and having large sizes (>153 μm).

Meanwhile, the bottom regime was affected by the coupling of upwelling-associated circulation and tidal oscillations (e.g., tidal flows), resulting in particle lateral transport and resuspension, respectively. Both mechanisms mainly entrained degraded particles finer than 63 μm. But the lateral transport carried more depleted $\delta^{13}C_{POC}$ because of microbial reworking or degradation. Overall, the POM in BNL was composed of particles<63 μm, degraded, and with depleted $\delta^{13}C_{POC}$, which might be interpreted as the "terrestrial" source. With multivariable constraints, the source of SPs in the regime can be clearly differentiated. Our work avoided temporal aliasing in the cause-and-effective observations between physical processes and biogeochemical properties of SPs. These findings contributed to the fundamental understanding of the physical forcing aspect of the biogeochemical cycling in river-dominated continental shelf systems like the NSCS.

Data availability statement

The raw data supporting the conclusions of this article will be made available by the authors, without undue reservation.

Author contributions

JL participated in the field work and was in charge of the data processing and manuscript preparation. JTL conceived and designed the study, supervised the work, and co-wrote the manuscript. Y-SL contributed to the POM analyses and provided consultation on the POM interpretation. C-TC and B-SW handled the nutrient analysis. All authors contributed to the article and approved the submitted version.

Funding

This study was funded by the R.O.C. Ministry of Science and Technology (MOST) under the grant numbers MOST 104-2611-M-110-011, MOST 105-2119-M-110-006, and MOST 106-2611-M-110-005.

Acknowledgments

We thank the captain and crew of R/V Ocean Researcher I for their assistance in the fieldwork. The Ocean Data Bank of MOST provided EK60 data. We acknowledge the use of imagery from NASA's Worldview application (https://worldview.earthdata.nasa.gov), which is part of the Earth Observing System Data and Information System (EOSDIS). We appreciate the help in analyzing NO_2^-, NO_3^-, PO_4^{3-}, and SiO_2 from the staff and students of C-TC's laboratory in the Department of Oceanography at National Sun Yat-sen University. We appreciate the work for NH_4^+ analyses from the members of Taiwan Ocean Research Institute.

Conflict of interest

The authors declare that the research was conducted in the absence of any commercial or financial relationships that could be construed as a potential conflict of interest.

Publisher's note

All claims expressed in this article are solely those of the authors and do not necessarily represent those of their affiliated organizations, or those of the publisher, the editors and the reviewers. Any product that may be evaluated in this article, or claim that may be made by its manufacturer, is not guaranteed or endorsed by the publisher.

Supplementary material

The Supplementary Material for this article can be found online at: https://www.frontiersin.org/articles/10.3389/fmars.2023.1156915/full#supplementary-material

References

Amiel, D., and Cochran, J. K. (2008). Terrestrial and marine POC fluxes derived from 234Th distributions and δ13C measurements on the Mackenzie shelf. *J. Geophys. Res. Ocean* 113, C03S06. doi: 10.1029/2007JC004260

Aminot, A., Kirkwood, D. S., and Kérouel, R. (1997). Determination of ammonia in seawater by the indophenol-blue method: evaluation of the ICES NUTS I/C 5 questionnaire. *Mar. Chem.* 56, 59–75. doi: 10.1016/S0304-4203(96)00080-1

Asada, T., Warner, B., and Aravena, R. (2005). Effects of the early stage of decomposition on change in carbon and nitrogen isotopes in sphagnum litter. *J. Plant Interact.* 1, 229–237. doi: 10.1080/17429140601056766

Bai, Y., Huang, T.-H., He, X., Wang, S.-L. L., Hsin, Y.-C., Wu, C.-R., et al. (2015). Intrusion of the pearl river plume into the main channel of the Taiwan strait in summer. *J. Sea Res.* 95, 1–15. doi: 10.1016/j.seares.2014.10.003

Bauer, J. E., Cai, W.-J., Raymond, P. A., Bianchi, T. S., Hopkinson, C. S., and Regnier, P. A. G. (2013). The changing carbon cycle of the coastal ocean. *Nature* 504, 61–70. doi: 10.1038/nature12857

Berhane, I., Sternberg, R. W., Kineke, G. C., Milligan, T. G., and Kranck, K. (1997). The variability of suspended aggregates on the Amazon continental shelf. *Cont. Shelf Res.* 17, 267–285. doi: 10.1016/S0278-4343(96)00033-7

Bianchi, T. S., Wysocki, L. A., Stewart, M., Filley, T. R., and McKee, B. A. (2007). Temporal variability in terrestrially-derived sources of particulate organic carbon in the lower Mississippi river and its upper tributaries. *Geochim. Cosmochim. Acta* 71, 4425–4437. doi: 10.1016/j.gca.2007.07.011

Bordovskiy, O. K. (1965). Accumulation of organic matter in bottom sediments. *Mar. Geol.* 3, 33–82. doi: 10.1016/0025-3227(65)90004-6

Cai, W.-J., Dai, M., Wang, Y., Zhai, W., Huang, T., Chen, S., et al. (2004). The biogeochemistry of inorganic carbon and nutrients in the pearl river estuary and the adjacent northern south China Sea. *Cont. Shelf Res.* 24, 1301–1319. doi: 10.1016/j.csr.2004.04.005

Cao, Z., Wang, D., Zhang, Z., Zhou, K., Liu, X., Wang, L., et al. (2020). Seasonal dynamics and export of biogenic silica in the upper water column of a large marginal sea, the northern south China Sea. *Prog. Oceanogr.* 188, 102421. doi: 10.1016/j.pocean.2020.102421

Castillo, C. R., Sarmento, H., Álvarez-Salgado, X. A., Gasol, J. M., and Marraséa, C. (2010). Production of chromophoric dissolved organic matter by marine phytoplankton. *Limnol. Oceanogr.* 55, 446–454. doi: 10.4319/lo.2010.55.1.0446

Chen, C.-T. A. (2002). Shelf-vs. dissolution-generated alkalinity above the chemical lysocline. *Deep Sea Res. Part II Top. Stud. Oceanogr.* 49, 5365–5375. doi: 10.1016/S0967-0645(02)00196-0

Chen, Z., Gong, W., Cai, H., Chen, Y., and Zhang, H. (2017). Dispersal of the pearl river plume over continental shelf in summer. *Estuar. Coast. Shelf Sci.* 194, 252–262. doi: 10.1016/j.ecss.2017.06.025

Chen, Y., and Zhao, H. (2021). Spatial distribution of the summer subsurface chlorophyll maximum in the north south China Sea. *PloS One* 16, e0248715. doi: 10.1371/journal.pone.0248715

Chivas, A. R., García, A., van der Kaars, S., Couapel, M. J. J., Holt, S., Reeves, J. M., et al. (2001). Sea-Level and environmental changes since the last interglacial in the gulf of carpentaria, Australia: an overview. *Quat. Int.* 83–85, 19–46. doi: 10.1016/S1040-6182(01)00029-5

Cloern, J. E., Canuel, E. A., and Harris, D. (2002). Stable carbon and nitrogen isotope composition of aquatic and terrestrial plants of the San Francisco bay estuarine system. *Limnol. Oceanogr.* 47, 713–729. doi: 10.4319/lo.2002.47.3.0713

Close, H. G., and Henderson, L. C. (2020). Open-ocean minima in δ13C values of particulate organic carbon in the lower euphotic zone. *Front. Mar. Sci.* 7. doi: 10.3389/fmars.2020.540165

Dagg, M., Benner, R., Lohrenz, S., and Lawrence, D. (2004). Transformation of dissolved and particulate materials on continental shelves influenced by large rivers: plume processes. *Cont. Shelf Res.* 24, 833–858. doi: 10.1016/j.csr.2004.02.003

D'Croz, L., and O'Dea, A. (2007). Variability in upwelling along the pacific shelf of Panama and implications for the distribution of nutrients and chlorophyll. *Estuar. Coast. Shelf Sci.* 73, 325–340. doi: 10.1016/j.ecss.2007.01.013

Dickson, M.-L., and Wheele, P. A. (1995). Nitrate uptake rates in a coastal upwelling regime: a comparison of PN-specific, absolute, and chl a-specific rates. *Limnol. Oceanogr.* 40, 533–543. doi: 10.4319/lo.1995.40.3.0533

Du, S., Ariful Islam, G. M., Xiang, R., and Yang, X. (2021). The dust deposition process and biogeochemical impacts in the northern south China Sea. *Asia-Pacific J. Atmos. Sci.* 57, 77–87. doi: 10.1007/s13143-019-00171-4

Du, X., and Liu, J. T. (2017). Particle dynamics of the surface, intermediate, and benthic nepheloid layers under contrasting conditions of summer monsoon and typhoon winds on the boundary between the Taiwan strait and East China Sea. *Prog. Oceanogr.* 156, 130–144. doi: 10.1016/j.pocean.2017.06.009

Du, X., Liu, J. T., Lee, J., Huang, P. S., Yang, R. J., and Jue, P. Z. (2022). Influence of sediment sources, water mass, and physical processes on the dynamics of flocs at a location between the mouth of a river and the head of a submarine canyon. *Mar. Geol.* 445, 106736. doi: 10.1016/j.margeo.2022.106736

Fanning, K. A., and Pilson, M. (1973). On the spectrophotometric determination of dissolved silica in natural waters. *Anal. Chem.* 45, 136–140. doi: 10.1021/ac60323a021

Feng, Y., Tang, Q., Li, J., Sun, J., and Zhan, W. (2021). Internal solitary waves observed on the continental shelf in the northern south China Sea from acoustic backscatter data. *Front. Mar. Sci.* 8. doi: 10.3389/fmars.2021.734075

Gan, J., and Allen, J. S. (2002). A modeling study of shelf circulation off northern California in the region of the coastal ocean dynamics experiment: response to relaxation of upwelling winds. *J. Geophys. Res. Ocean.* 107, 6–31. doi: 10.1029/2000JC000768

Gan, J., Cheung, A., Guo, X., and Li, L. (2009a). Intensified upwelling over a widened shelf in the northeastern south China Sea. *J. Geophys. Res. Ocean.* 114, 1–15. doi: 10.1029/2007JC004660

Gan, J., Li, L., Wang, D., and Guo, X. (2009b). Interaction of a river plume with coastal upwelling in the northeastern south China Sea. *Cont. Shelf Res.* 29, 728–740. doi: 10.1016/j.csr.2008.12.002

Gan, J., Lu, Z., Dai, M., Cheung, A. Y. Y., Liu, H., and Harrison, P. (2010). Biological response to intensified upwelling and to a river plume in the northeastern south China Sea: a modeling study. *J. Geophys. Res. Ocean.* 115, 1–19. doi: 10.1029/2009JC005569

Gao, C., Fu, M., Song, H., Wang, L., Wei, Q., Sun, P., et al. (2018). Phytoplankton pigment pattern in the subsurface chlorophyll maximum in the south Java coastal upwelling system, Indonesia. *Acta Oceanol. Sin.* 37, 97–106. doi: 10.1007/s13131-018-1342-x

Gao, L., Li, D., and Ishizaka, J. (2014). Stable isotope ratios of carbon and nitrogen in suspended organic matter: seasonal and spatial dynamics along the changjiang (Yangtze river) transport pathway. *J. Geophys. Res. Biogeosci.* 119, 1717–1737. doi: 10.1002/2013JG002487

Gao, S., Liu, Y., Yang, Y., Liu, P. J., Zhang, Y., and Wang, Y. P. (2015). Evolution status of the distal mud deposit associated with the pearl river, northern south China Sea continental shelf. *J. Asian Earth Sci.* 114, 562–573. doi: 10.1016/j.jseaes.2015.07.024

Garvine, R. W., and Monk, J. D. (1974). Frontal structure of a river plume. *J. Geophys. Res.* 79, 2251–2259. doi: 10.1029/JC079i015p02251

Gibbs, R. J. (1973). Mechanisms of trace metal transport in rivers. *Science* 180 (80), 71–73. doi: 10.1126/science.180.4081.71

Gibbs, R. J. (1977). *Distribution and transport of suspended particulate material of the Amazon river in the ocean*. Ed. M.B.T.-E.P. WILEY (USA: Academic Press), 35–47. doi: 10.1016/B978-0-12-751802-2.50011-4

Gibbs, R. J., and Konwar, L. (1986). Coagulation and settling of Amazon river suspended sediment. *Cont. Shelf Res.* 6, 127–149. doi: 10.1016/0278-4343(86)90057-9

Gireeshkumar, T. R., Deepulal, P. M., and Chandramohanakumar, N. (2013). Distribution and sources of sedimentary organic matter in a tropical estuary, south west coast of India (Cochin estuary): a baseline study. *Mar. pollut. Bull.* 66, 239–245. doi: 10.1016/j.marpolbul.2012.10.002

Gong, F., Li, G., Wang, Y., Liu, Q., Huang, F., Yin, K., et al. (2020). Spatial shifts in size structure, phylogenetic diversity, community composition and abundance of small eukaryotic plankton in a coastal upwelling area of the northern south China Sea. *J. Plankton Res.* 42, 650–667. doi: 10.1093/plankt/fbaa046

Goni, M. A., Monacci, N., Gisewhite, R., Ogston, A., Crockett, J., and Nittrouer, C. (2006). Distribution and sources of particulate organic matter in the water column and sediments of the fly river delta, gulf of Papua (Papua new Guinea). *Estuar. Coast. Shelf Sci.* 69, 225–245. doi: 10.1016/j.ecss.2006.04.012

Goñi, M. A., Yunker, M. B., Macdonald, R. W., and Eglinton, T. I. (2000). Distribution and sources of organic biomarkers in arctic sediments from the Mackenzie river and Beaufort shelf. *Mar. Chem.* 71, 23–51. doi: 10.1016/S0304-4203(00)00037-2

Gregory, J. (1998). The role of floc density in solid-liquid separation. *Filtr. Sep.* 35, 366–367. doi: 10.1016/S0015-1882(97)87417-4

Guo, W., Jia, G., Ye, F., Xiao, H., and Zhang, Z. (2019). Lipid biomarkers in suspended particulate matter and surface sediments in the pearl river estuary, a subtropical estuary in southern China. *Sci. Total Environ.* 646, 416–426. doi: 10.1016/j.scitotenv.2018.07.159

Guo, W., Ye, F., Xu, S., and Jia, G. (2015). Seasonal variation in sources and processing of particulate organic carbon in the pearl river estuary, south China. *Estuar. Coast. Shelf Sci.* 167, 540–548. doi: 10.1016/j.ecss.2015.11.004

Haines, E. B. (1976). Stable carbon isotope ratios in the biota, soils and tidal water of a Georgia salt marsh. *Estuar. Coast. Mar. Sci.* 4, 609–616. doi: 10.1016/0302-3524(76)90069-4

Harmelin-Vivien, M., Dierking, J., Bănaru, D., Fontaine, M. F., and Arlhac, D. (2010). Seasonal variation in stable c and n isotope ratios of the Rhone river inputs to the Mediterranean Sea, (2004–2005). *Biogeochemistry* 100, 139–150. doi: 10.1007/s10533-010-9411-z

Harrison, P. J., Yin, K., Lee, J. H. W., Gan, J., and Liu, H. (2008). Physical–biological coupling in the pearl river estuary. *Cont. Shelf Res.* 28, 1405–1415. doi: 10.1016/j.csr.2007.02.011

Heise, B., Bobertz, B., Tang, C., Harff, J., and Zhou, D. (2013). Surface sediments of the pearl river estuary (South China Sea) – spatial distribution of sedimentological / geochemical properties and environmental interpretation. *J. Coast. Res.* 66, 34–48. doi: 10.2112/SI_66_4

Ho, Q. N., Fettweis, M., Spencer, K. L., and Lee, B. J. (2022). Flocculation with heterogeneous composition in water environments: a review. *Water Res.* 213, 118147. doi: 10.1016/j.watres.2022.118147

Hong, H., Zheng, Q., Jianyu, H. U., Chen, Z., Chunyan, L. I., Jiang, Y., et al. (2009). Three-dimensional structure of a low salinity tongue in the southern Taiwan strait observed in the summer of 2005. *Acta Oceanol. Sin.* 28, 1–7.

Hoshika, A., Tanimoto, T., Mishima, Y., Iseki, K., and Okamura, K. (2003). Variation of turbidity and particle transport in the bottom layer of the East China Sea. *Deep Sea Res. Part II Top. Stud. Oceanogr.* 50, 443–455. doi: 10.1016/S0967-0645(02)00462-9

Hsu, R. T., and Liu, J. T. (2010). *In-situ* Estimations of the density and porosity of flocs of varying sizes in a submarine canyon. *Mar. Geol.* 276, 105–109. doi: 10.1016/j.margeo.2010.07.003

Hu, J., Peng, P., Jia, G., Mai, B., and Zhang, G. (2006). Distribution and sources of organic carbon, nitrogen and their isotopes in sediments of the subtropical pearl river estuary and adjacent shelf, southern China. *Mar. Chem.* 98, 274–285. doi: 10.1016/j.marchem.2005.03.008

Huang, W. J., Kao, K. J., Lin, Y. S., Arthur Chen, C. T., and Liu, J. T. (2020). Daily to weekly impacts of mixing and biological activity on carbonate dynamics in a large river-dominated shelf. *Estuar. Coast. Shelf Sci.* 245, 106914. doi: 10.1016/j.ecss.2020.106914

Huang, C., Lao, Q., Chen, F., Zhang, S., Chen, C., Bian, P., et al. (2021). Distribution and sources of particulate organic matter in the northern south China Sea: implications of human activity. *J. Ocean Univ. China* 20, 1136–1146. doi: 10.1007/s11802-021-4807-z

Isobe, A., and Matsuno, T. (2008). Long-distance nutrient-transport process in the changjiang river plume on the East China Sea shelf in summer. *J. Geophys. Res. Ocean.* 113, C04006. doi: 10.1029/2007JC004248

Ivančič, I., and Degobbis, D. (1984). An optimal manual procedure for ammonia analysis in natural waters by the indophenol blue method. *Water Res.* 18, 1143–1147. doi: 10.1016/0043-1354(84)90230-6

Jarvis, P., Jefferson, B., Gregory, J., and Parsons, S. A. (2005). A review of floc strength and breakage. *Water Res.* 39, 3121–3137. doi: 10.1016/j.watres.2005.05.022

Jeandel, C. (2016). Overview of the mechanisms that could explain the 'Boundary exchange' at the land–ocean contact. *Philos. Trans. R. Soc A Math. Phys. Eng. Sci.* 374, 20150287. doi: 10.1098/rsta.2015.0287

Jia, Y., Tian, Z., Shi, X., Liu, J. P., Chen, J., Liu, X., et al. (2019). Deep-sea sediment resuspension by internal solitary waves in the northern south China Sea. *Sci. Rep.* 9, 1–8. doi: 10.1038/s41598-019-47886-y

Jiang, Z., Chen, J., Zhou, F., Shou, L., Chen, Q., Tao, B., et al. (2015). Controlling factors of summer phytoplankton community in the changjiang (Yangtze river) estuary and adjacent East China Sea shelf. *Cont. Shelf Res.* 101, 71–84. doi: 10.1016/j.csr.2015.04.009

JPL MUR MEaSUREs Project (2015). *GHRSST level 4 MUR global foundation Sea surface temperature analysis (v4.1)*. (CA, USA: PO.DAAC). doi: 10.5067/GHGMR-4FJ04

Kämpf, J., and Chapman, P. (2016). *Seasonal wind-driven coastal upwelling systems BT - upwelling systems of the world: a scientific journey to the most productive marine ecosystems*. Eds. J. Kämpf and P. Chapman (Cham: Springer International Publishing), 315–361. doi: 10.1007/978-3-319-42524-5_8

Kay, S. M. (1988). *Modern spectral estimation* (Englewood Cliffs, NJ: Prentice-Hall).

Ko, C.-Y., Hsin, Y.-C., and Jeng, M.-S. (2020). Global distribution and cleanup opportunities for macro ocean litter: a quarter century of accumulation dynamics under windage effects. *Environ. Res. Lett.* 15, 104063. doi: 10.1088/1748-9326/abae29

Kuehl, S. A., DeMaster, D. J., and Nittrouer, C. A. (1986). Nature of sediment accumulation on the Amazon continental shelf. *Cont. Shelf Res.* 6, 209–225. doi: 10.1016/0278-4343(86)90061-0

Lacan, F., and Jeandel, C. (2005). Neodymium isotopes as a new tool for quantifying exchange fluxes at the continent–ocean interface. *Earth Planet. Sci. Lett.* 232, 245–257. doi: 10.1016/j.epsl.2005.01.004

Lamb, K. G., and Warn-Varnas, A. (2015). Two-dimensional numerical simulations of shoaling internal solitary waves at the ASIAEX site in the south China Sea. *Nonlinear Process. Geophys.* 22, 289–312. doi: 10.5194/npg-22-289-2015

Lamb, A. L., Wilson, G. P., and Leng, M. J. (2006). A review of coastal palaeoclimate and relative sea-level reconstructions using δ13C and C/N ratios in organic material. *Earth-Sci. Rev.* 75, 29–57. doi: 10.1016/j.earscirev.2005.10.003

Lee, J., Liu, J. T., Hung, C. C., Lin, S., and Du, X. (2016). River plume induced variability of suspended particle characteristics. *Mar. Geol.* 380, 219–230. doi: 10.1016/j.margeo.2016.04.014

Lee, J., Liu, J. T., Lee, I.-H. H., Fu, K.-H. H., Yang, R. J., Gong, W., et al. (2021). Encountering shoaling internal waves on the dispersal pathway of the pearl river plume in summer. *Sci. Rep.* 11, 999. doi: 10.1038/s41598-020-80215-2

Lee, J., Yang, R. J., Lin, H.-L., Chen, Y.-C., Cai-Li, R.-Y., Ren, H., et al. (2022). Sedimentary anthropogenic carbon signals from the Western pacific margin for the last century. *Front. Earth Sci.* 9. doi: 10.3389/feart.2021.795519

Li, Q. P., Ge, Z., Liu, Z., Zhou, W., Shuai, Y., and Wu, Z. (2021). Transparent exopolymer particles in a coastal frontal zone of the northern south China Sea and the associated biogeochemical implications. *J. Geophys. Res. Biogeosci.* 126, e2020JG005893. doi: 10.1029/2020JG005893

Linders, T., Infantes, E., Joyce, A., Karlsson, T., Ploug, H., Hassellöv, M., et al. (2018). Particle sources and transport in stratified Nordic coastal seas in the anthropocene. *Elem. Sci. Anthr.* 6, 29. doi: 10.1525/elementa.149

Liu, M., Hou, L. J., Xu, S. Y., Ou, D. N., Yang, Y., Yu, J., et al. (2006). Organic carbon and nitrogen stable isotopes in the intertidal sediments from the Yangtze estuary, China. *Mar. pollut. Bull.* 52, 1625–1633. doi: 10.1016/j.marpolbul.2006.06.008

Liu, J. T., Hsu, R. T., Yang, R. J., Wang, Y. P., Wu, H., Du, X., et al. (2018). A comprehensive sediment dynamics study of a major mud belt system on the inner shelf along an energetic coast. *Sci. Rep.* 8, 4229. doi: 10.1038/s41598-018-22696-w

Liu, J. T., Huang, B., Chang, Y., Du, X., Liu, X., Yang, R. J., et al. (2019). Three-dimensional coupling between size-fractionated chlorophyll-a, POC and physical processes in the Taiwan strait in summer. *Prog. Oceanogr.* 176, 102129. doi: 10.1016/j.pocean.2019.102129

Liu, J. T., Hung, J.-J., Lin, H.-L., Huh, C.-A., Lee, C.-L., Hsu, R. T., et al. (2009). From suspended particles to strata: the fate of terrestrial substances in the gaoping (Kaoping) submarine canyon. *J. Mar. Syst.* 76, 417–432. doi: 10.1016/j.jmarsys.2008.01.010

Liu, K.-K., Kao, S.-J., Hu, H.-C., Chou, W.-C., Hung, G.-W., and Tseng, C.-M. (2007). Carbon isotopic composition of suspended and sinking particulate organic matter in the northern south China Sea–from production to deposition. *Deep Sea Res. Part II Top. Stud. Oceanogr.* 54, 1504–1527. doi: 10.1016/j.dsr2.2007.05.010

Liu, J. T., Lee, J., Yang, R. J., Du, X., Li, A., Lin, Y.-S., et al. (2021). Coupling between physical processes and biogeochemistry of suspended particles over the inner shelf mud in the East China Sea. *Mar. Geol.* 442, 106657. doi: 10.1016/j.margeo.2021.106657

Liu, J. H., Yang, S. L., Zhu, Q., and Zhang, J. (2014). Controls on suspended sediment concentration profiles in the shallow and turbid Yangtze estuary. *Cont. Shelf Res.* 90, 96–108. doi: 10.1016/j.csr.2014.01.021

Liu, Z., Zhao, Y., Colin, C., Stattegger, K., Wiesner, M. G., Huh, C.-A., et al. (2016). Source-to-sink transport processes of fluvial sediments in the south China Sea. *Earth-Sci. Rev.* 153, 238–273. doi: 10.1016/j.earscirev.2015.08.005

Lorthiois, T., Doxaran, D., and Chami, M. (2012). Daily and seasonal dynamics of suspended particles in the rhône river plume based on remote sensing and field optical measurements. *Geo-Marine Lett.* 32, 89–101. doi: 10.1007/s00367-012-0274-2

Lu, Z., Gan, J., Dai, M., and Cheung, A. Y. Y. (2010). The influence of coastal upwelling and a river plume on the subsurface chlorophyll maximum over the shelf of the northeastern south China Sea. *J. Mar. Syst.* 82, 35–46. doi: 10.1016/j.jmarsys.2010.03.002

Malakoff, D. (1998). Death by suffocation in the gulf of Mexico. *Science* 281, 190–192. doi: 10.1126/science.281.5374.190

McKee, B. A., Aller, R. C., Allison, M. A., Bianchi, T. S., and Kineke, G. C. (2004). Transport and transformation of dissolved and particulate materials on continental margins influenced by major rivers: benthic boundary layer and seabed processes. *Cont. Shelf Res.* 24, 899–926. doi: 10.1016/j.csr.2004.02.009

Meyers, P. A. (1994). Preservation of elemental and isotopic source identification of sedimentary organic matter. *Chem. Geol.* 114, 289–302. doi: 10.1016/0009-2541(94)90059-0

Middelburg, J. J., and Nieuwenhuize, J. (1998). Carbon and nitrogen stable isotopes in suspended matter and sediments from the schelde estuary. *Mar. Chem.* 60, 217–225. doi: 10.1016/S0304-4203(97)00104-7

Mittelstaedt, E. (1991). The ocean boundary along the northwest African coast: circulation and oceanographic properties at the sea surface. *Prog. Oceanogr.* 26, 307–355. doi: 10.1016/0079-6611(91)90011-A

Murphy, J., and Riley, J. P. (1962). A modified single solution method for the determination of phosphate in natural waters. *Anal. Chim. Acta* 27, 31–36. doi: 10.1016/S0003-2670(00)88444-5

Myklestad, S. M. (2005). Dissolved organic carbon from phytoplankton. *Mar. Chem.* 5, 111–148. doi: 10.1007/10683826_5

Neumeier, U., Ferrarin, C., Amos, C. L., Umgiesser, G., and Li, M. Z. (2008). Sedtrans05: an improved sediment-transport model for continental shelves and coastal waters with a new algorithm for cohesive sediments. *Comput. Geosci.* 34, 1223–1242. doi: 10.1016/j.cageo.2008.02.007

Nittrouer, C. A., and DeMaster, D. J. (1996). The Amazon shelf setting: tropical, energetic, and influenced by a large river. *Cont. Shelf Res.* 16, 553–573. doi: 10.1016/0278-4343(95)00069-0

O'Hara Murray, R. B., Hodgson, D. M., and Thorne, P. D. (2012). Wave groups and sediment resuspension processes over evolving sandy bedforms. *Cont. Shelf Res.* 46, 16–30. doi: 10.1016/j.csr.2012.02.011

Pai, S.-C., Gong, G.-C., and Liu, K.-K. (1993). Determination of dissolved oxygen in seawater by direct spectrophotometry of total iodine. *Mar. Chem.* 41, 343–351. doi: 10.1016/0304-4203(93)90266-Q

Passow, U., de la Rocha, C. L., Fairfield, C., and Schmidt, K. (2014). Aggregation as a function of and mineral particles. *Limnol. Oceanogr.* 59, 532–547. doi: 10.4319/lo.2014.59.2.0532

Passow, U., Shipe, R. F., Murray, A., Pak, D. K., Brzezinski, M. A., and Alldredge, A. L. (2001). The origin of transparent exopolymer particles (TEP) and their role in the sedimentation of particulate matter. *Cont. Shelf Res.* 21, 327–346. doi: 10.1016/S0278-4343(00)00101-1

Pawlowicz, R., Beardsley, B., and Lentz, S. (2002). Classical tidal harmonic analysis including error estimates in MATLAB using T_TIDE. *Comput. Geosci.* 28, 929–937. doi: 10.1016/S0098-3004(02)00013-4

Peterson, B., Fry, B., Hullar, M., Saupe, S., and Wright, R. (1994). The distribution and stable carbon isotopic composition of dissolved organic carbon in estuaries. *Estuaries* 17, 111–121. doi: 10.2307/1352560

Rabiner, R. L., and Gold, B. (1975). *Theory and application of digital signal processing* (Englewood Cliffs, NJ: Prentice-Hall).

Ran, Y., and Zhang, Y. (2015). "Sources, early diagenesis, and structure of organic matter in the pearl river delta," in *Labile org. matter–chemical compos. funct. significance soil environ* (USA: SSSA Special Publications). doi: 10.2136/sssaspecpub62.2014.0047

Raymond, P. A., and Bauer, J. E. (2001). Use of 14C and 13C natural abundances for evaluating riverine, estuarine, and coastal DOC and POC sources and cycling: a review and synthesis. *Org. Geochem.* 32, 469–485. doi: 10.1016/S0146-6380(00)00190-X

Rixen, T., Gaye, B., Emeis, K.-C., and Ramaswamy, V. (2019). The ballast effect of lithogenic matter and its influences on the carbon fluxes in the Indian ocean. *Biogeosciences* 16, 485–503. doi: 10.5194/bg-16-485-2019

Schidlowski, M., Hayes, J. M., and Kaplan, I. R. (1983). Isotopic inferences of ancient biochemis-tries: Carbon, sulfur, hydrogen, and nitrogen. *Earth's Earliest Biosphere: Its Origin and Evolution*, ed J. W. Schopf (New York: Princeton Univ Press), pp 149–186

Sherr, E. B. (1982). Carbon isotope composition of organic seston and sediments in a Georgia salt marsh estuary. *Geochim. Cosmochim. Acta* 46, 1227–1232. doi: 10.1016/0016-7037(82)90007-2

Strickland, J. D. H., and Parsons, T. R. (1972). *A Practical Handbook of Seawater Analysis. 2nd* edition. Ottawa, Canada, Fisheries Research Board of Canada, 310pp. (Bulletin Fisheries Research Board of Canada, Nr. 167 (2nd ed)). doi: 10.25607/OBP-1791.

Su, L., Yuan, Z., Fung, J. C. H., and Lau, A. K. H. (2015). A comparison of HYSPLIT backward trajectories generated from two GDAS datasets. *Sci. Total Environ.* 506–507, 527–537. doi: 10.1016/j.scitotenv.2014.11.072

Thorne, P. D., Davies, A. G., and Bell, P. S. (2009). Observations and analysis of sediment diffusivity profiles over sandy rippled beds under waves. *J. Geophys. Res. Ocean.* 114, C02023. doi: 10.1029/2008JC004944

Tian, Y., Huang, W., Chen, Z., Wang, S., Zhu, X., and Yan, W. (2022). Characteristics of sound speed in four seafloor sedimentary types in the south China Sea. *Arab. J. Geosci.* 15, 596. doi: 10.1007/s12517-022-09714-y

Tian, Z., Liu, Y., Zhang, X., Zhang, Y., and Zhang, M. (2022). Formation mechanisms and characteristics of the marine nepheloid layer: a review. *Water* 14, 678. doi: 10.3390/w14050678

Tolman, H. L. (1991). A third-generation model for wind waves on slowly varying, unsteady, and inhomogeneous depths and currents. *J. Phys. Oceanogr.* 21, 782–797. doi: 10.1175/1520-0485(1991)021<0782:ATGMFW>2.0.CO;2

Turner, A., and Millward, G. E. (2002). Suspended particles: their role in estuarine biogeochemical cycles. *Estuar. Coast. Shelf Sci.* 55, 857–883. doi: 10.1006/ecss.2002.1033

Van Rijn, L. C. (1993). *Principle of sediment transport in Rivers,Estuaries and coastal seas* (Amsterdam: Aqua Publications).

Wang, D., Shu, Y., Xue, H., Hu, J., Chen, J., Zhuang, W., et al. (2014). Relative contributions of local wind and topography to the coastal upwelling intensity in the northern south China Sea. *J. Geophys. Res. Ocean.* 119, 2550–2567. doi: 10.1002/2013JC009172

Wang, G., Zhou, W., Cao, W., Yin, J., Yang, Y., Sun, Z., et al. (2011). Variation of particulate organic carbon and its relationship with bio-optical properties during a phytoplankton bloom in the pearl river estuary. *Mar. pollut. Bull.* 62, 1939–1947. doi: 10.1016/j.marpolbul.2011.07.003

Weber, S. C., Carpenter, E. J., Coles, V. J., Yager, P. L., Goes, J., and Montoya, J. P. (2017). Amazon River influence on nitrogen fixation and export production in the western tropical north Atlantic. *Limnol. Oceanogr.* 62, 618–631. doi: 10.1002/lno.10448

Weeks, A. R., Simpson, J. H., and Bowers, D. (1993). The relationship between concentrations of suspended particulate material and tidal processes in the Irish Sea. *Cont. Shelf Res.* 13, 1325–1334. doi: 10.1016/0278-4343(93)90086-D

Wei, B., Mollenhauer, G., Hefter, J., Grotheer, H., and Jia, G. (2020). Dispersal and aging of terrigenous organic matter in the pearl river estuary and the northern south China Sea shelf. *Geochim. Cosmochim. Acta* 282, 324–339. doi: 10.1016/j.gca.2020.04.032

Welch, P. (1967). The use of fast Fourier transform for the estimation of power spectra: a method based on time averaging over short, modified periodograms. *IEEE Trans. Audio Electroacoust.* 15, 70–73. doi: 10.1109/TAU.1967.1161901

Wen, L.-S., Lee, C.-P., Lee, W.-H., and Chuang, A. (2018). An ultra-clean multilayer apparatus for collecting size fractionated marine plankton and suspended particles. *J. Vis. Exp* 134. doi: 10.3791/56811

Wright, L. D., and Coleman, J. M. (1973). Variations in morphology of major river deltas as functions of ocean wave and river discharge Regimes1. *Am. Assoc. Pet. Geol. Bull.* 57, 370–398. doi: 10.1306/819A4274-16C5-11D7-8645000102C1865D

Wright, L. D., and Nittrouer, C. A. (1995). Dispersal of river sediments in coastal seas: six contrasting cases. *Estuaries* 18, 494–508. doi: 10.2307/1352367

Wu, C. S., Yang, S., Huang, S., and Mu, J. (2016). Delta changes in the pearl river estuary and its response to human activities, (1954–2008). *Quat. Int.* 392, 147–154. doi: 10.1016/j.quaint.2015.04.009

Wu, C. S., Yang, S. L., and Lei, Y. (2012). Quantifying the anthropogenic and climatic impacts on water discharge and sediment load in the pearl river (Zhujiang), china, (1954–2009). *J. Hydrol.* 452–453, 190–204. doi: 10.1016/j.jhydrol.2012.05.064

Xu, Y., Dai, M., Zhai, W., Yuan, D., Liu, J., Sun, Z., et al. (2009). Short-term dynamics of nutrients influenced by upwelling in a small oligotrophic coastal ecosystem, gan bay, in the northwest Philippines. *Prog. Nat. Sci.* 19, 595–601. doi: 10.1016/j.pnsc.2008.10.005

Xu, J., Yin, K., He, L., Yuan, X., Ho, A. Y. T., and Harrison, P. J. (2008). Phosphorus limitation in the northern south China Sea during late summer: influence of the pearl river. *Deep Sea Res. Part I Oceanogr. Res. Pap.* 55, 1330–1342. doi: 10.1016/j.dsr.2008.05.007

Yang, R. J., Liu, J. T., Su, C.-C., Chang, Y., Xu, J. J., and Lui, H.-K. (2021). Land-ocean interaction affected by the monsoon regime change in Western Taiwan strait. *Front. Mar. Sci.* 8. doi: 10.3389/fmars.2021.735242

Yin, K. D., Qian, P. Y., Wu, M. C. S., Chen, J. C., Huang, L., Song, X., et al. (2001). Shift from p to n limitation of phytoplankton growth across the pearl river estuarine plume during summer. *Mar. Ecol. Prog. Ser.* 221, 17–28. doi: 10.3354/meps221017

Yu, X., Xu, J., Long, A., Li, R., Shi, Z., and Li, Q. P. (2020). Carbon-to-chlorophyll ratio and carbon content of phytoplankton community at the surface in coastal waters adjacent to the zhujiang river estuary during summer. *Acta Oceanol. Sin.* 39, 123–131. doi: 10.1007/s13131-020-1556-6

Yu, F., Zong, Y., Lloyd, J. M., Huang, G., Leng, M. J., Kendrick, C., et al. (2010). Bulk organic δ13C and C/N as indicators for sediment sources in the pearl river delta and estuary, southern China. *Estuar. Coast. Shelf Sci.* 87, 618–630. doi: 10.1016/j.ecss.2010.02.018

Zhang, H., Cheng, W., Chen, Y., Yu, L., and Gong, W. (2018). Controls on the interannual variability of hypoxia in a subtropical embayment and its adjacent waters in the guangdong coastal upwelling system, northern south China Sea. *Ocean Dyn.* 68, 923–938. doi: 10.1007/s10236-018-1168-2

Zhang, J., Li, H., Xuan, J., Wu, Z., Yang, Z., Wiesner, M. G., et al. (2019). Enhancement of mesopelagic sinking particle fluxes due to upwelling, aerosol deposition, and monsoonal influences in the northwestern south China Sea. *J. Geophys. Res. Ocean.* 124, 99–112. doi: 10.1029/2018JC014704

Zhang, W., Mu, S., Zhang, Y., and Chen, K. (2012). Seasonal and interannual variations of flow discharge from pearl river into sea. *Water Sci. Eng.* 5, 399–409. doi: 10.3882/j.issn.1674-2370.2012.04.004

Zhang, W., Zheng, J., Xiaomei, J., Hoitink, A. J. F., van der Vegt, M., and Zhu, Y. (2013). Surficial sediment distribution and the associated net sediment transport pattern retain–>in the pearl river estuary, south China. *Cont. Shelf Res.* 61–62, 41–51. doi: 10.1016/j.csr.2013.04.011

Zhao, L., and Gao, L. (2019). Dynamics of dissolved and particulate organic matter in the changjiang (Yangtze river) estuary and the adjacent East China Sea shelf. *J. Mar. Syst.* 198, 103188. doi: 10.1016/j.jmarsys.2019.103188

Zhi, H., Wu, H., Wu, J., Zhang, W., and Wang, Y. (2022). River plume rooted on the Sea-floor: seasonal and spring-neap variability of the pearl river plume front. *Front. Mar. Sci.* 9. doi: 10.3389/fmars.2022.791948

Zhong, Y., Chen, Z., Li, L., Liu, J., Li, G., Zheng, X., et al. (2017). Bottom water hydrodynamic provinces and transport patterns of the northern south China Sea: evidence from grain size of the terrigenous sediments. *Cont. Shelf Res.* 140, 11–26. doi: 10.1016/j.csr.2017.01.023

Zu, T., and Gan, J. (2015). A numerical study of coupled estuary–shelf circulation around the pearl river estuary during summer: responses to variable winds, tides and river discharge. *Deep Sea Res. Part II Top. Stud. Oceanogr.* 117, 53–64. doi: 10.1016/j.dsr2.2013.12.010

Zu, T., Wang, D., Gan, J., and Guan, W. (2014). On the role of wind and tide in generating variability of pearl river plume during summer in a coupled wide estuary and shelf system. *J. Mar. Syst.* 136, 65–79. doi: 10.1016/j.jmarsys.2014.03.005